Journal of Marine Systems 203 (2020) 103262

Contents lists available at ScienceDirect

Journal of Marine Systems

journal homepage: www.elsevier.com/locate/jmarsys

Interannual Coastal Trapped Waves in the Angola-Benguela Upwelling System and Benguela Niño and Niña events

Marie-Lou Bachèlery[a,b,*], Serena Illig[c,a], Mathieu Rouault[a,b]

[a] Department of Oceanography, MARE Institute, LMI ICEMASA, University of Cape Town, Rondebosch, South Africa.
[b] Nansen-Tutu Centre for Marine Environmental Research, University of Cape Town, Rondebosch, South Africa
[c] Laboratoire d'Etudes en Géophysique et Océanographie Spatiale (LEGOS), CNRS/IRD/UPS/CNES, Toulouse, France

ARTICLE INFO

Keywords:
Coastal Trapped Waves
Benguela Niño-Niña events
Angola-Benguela Upwelling System
Equatorial dynamics

ABSTRACT

We investigate the dynamics of the interannual Coastal Trapped Waves (CTW) propagations along the south-western African coast and their role in triggering Benguela Niño and Niña events from 1958 to 2008. Using regional ocean model sensitivity experiments, we track equatorially-forced CTW down to the Southern Benguela Upwelling System (SBUS), where they account for 70% of the coastal sea level anomalies (SLA), temperature, and salinity variability. We then decompose the model coastal variability into individual CTW modal contributions and identify periods of energetic downwelling and upwelling propagations. A composite analysis allows for documenting and quantifying the oceanic response (circulation, temperature, and salinity) on the shelf during the passage of remotely-forced CTW. Results reveal that North of ~19°S, the coastal interannual variability is dominated by the second and third CTW modes. In the BUS, their amplitudes decrease and the interannual fluctuations are largely explained (> 70%) by the faster and weakly-dissipative first CTW mode. This dynamic explains the peculiar propagative pattern associated with SLA propagations, in which equatorially-forced fluctuations in the SBUS peak before the waves imprint the variability at ~19°S. The impact of CTW on the temperature in the SBUS is drastically lower than in the NBUS and Angolan regions. At last, we show that 71% of the extreme Benguela Niño and Niña events, in the surface layer, are associated with remotely-forced CTW propagations. The coherence between our CTW index and these extreme events increases when detecting temperature anomalies in the sub-surface rather than at the sea surface.

1. Introduction

Dominated by the upwelling dynamics, the near-shore ocean along the south-west coast of Africa is a very productive region (Carr and Kearns, 2003; Chavez and Messié, 2009; Quiñones, 2010; Lachkar and Gruber, 2012). This region comprises of three alongshore sub-systems almost coinciding with the political boundaries of coastal countries (Fig. 1a) and characterised by different ocean dynamics, physico-chemical characteristics and biota (Shillington, 1998; Shillington et al., 2006; Hutchings et al., 2009; Ostrowski et al., 2009). The Angolan sub-system (~5°S–17°S; Fig. 1a) is under the influence of relatively weak surface winds (Hellerman, 1980) and the Angolan poleward alongshore surface current that transports the warm equatorial waters southward (Moroshkin et al., 1970; Dias, 1983a, 1983b; Kopte et al., 2017). A small coastal upwelling is reported, which is supported by coastal wave propagations originating from the equator (Berrit, 1976; Picaut, 1983; Ostrowski et al., 2009; Kopte et al., 2017). The two others sub-systems form the Benguela Upwelling System (BUS), characterised by strong prevailing equatorward alongshore wind, intense upwelling dynamics and the equatorward Benguela Jet (Shannon and Nelson, 1996; Shillington, 1998; Shillington et al., 2006). They are separated by the major perennial upwelling cell of Lüderitz at ~27°S (Lutjeharms and Meeuwis, 1987) that has been shown to create a barrier for the movement of several marine species (Agenbag and Shannon, 1988; Duncombe-Rae, 2005; van der Lingen et al., 2006; Lett et al., 2007). The Northern part of the BUS (NBUS - ~17°S–26°S; Fig. 1a) hosts a permanent upwelling (Boyer et al., 2000), while in the southern part of the BUS (SBUS - ~28°S–33°S; Fig. 1a), the upwelling is seasonal (Strub et al., 1998; Hutchings et al., 2009). In the three sub-system regions, small-scale or industrial fisheries are widely developed along the shore and are critical for economic security and the employment of local coastal communities (Hutchings et al., 2009; Sowman and Cardoso, 2010; FAO, 2011).

The coastal upwelling in the three sub-systems also exhibits a high

* Corresponding author at: University of Cape Town (UCT), Department of Oceanography, Private Bag X3, Rondebosch 7701, South Africa.
E-mail address: bachelery.marielou@gmail.com (M.-L. Bachèlery).

https://doi.org/10.1016/j.jmarsys.2019.103262
Received 29 March 2019; Received in revised form 25 October 2019; Accepted 1 November 2019
Available online 18 November 2019

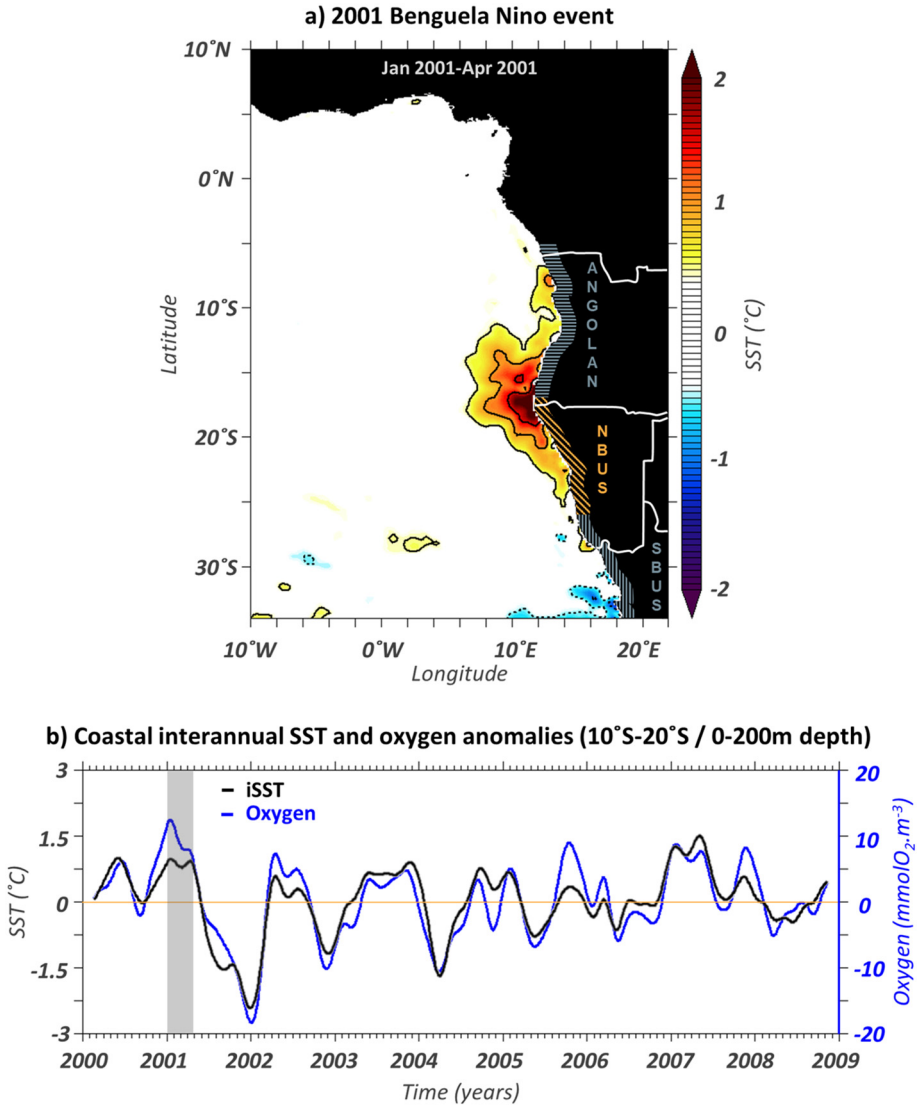

Fig. 1. a) Map of **i**nterannual **S**ea **S**urface **T**emperature (**iSST**; °C) from the GHRSST remotely-sensed observation (see the Supporting information for more details about the data) averaged during the peak phase of the 2001 Benguela Niño event (*cf.* grey vertical band in Fig. 1b). Black contours interval is 0.5 °C. White contours inland delineate the Angola, Namibia, and South Africa countries borders. The position of the three subsystems (Angolan, NBUS and SBUS) is highlighted by the hatched lines in the African continent. b) Time series of iSST (black line; °C) and oxygen anomalies (averaged in the first 200 m; blue line; $mmolO_2.m^{-3}$) from the $ROMS_{REF}$ simulation in Bachèlery et al. (2016). Model outputs have been averaged over a 0.5° coastal band from 10°S to 20°S. (For interpretation of the references to colour in this figure legend, the reader is referred to the web version of this article.)

variability from sub-monthly to interannual timescales that has been intensively studied based on observed data and model outputs (Polo et al., 2008; Goubanova et al., 2013; Lübbecke et al., 2010; Rouault, 2012; Imbol Koungue et al., 2017; Illig et al., 2018a, 2018b; Illig and Bachèlery, 2019). These fluctuations strongly affect the marine biodiversity (Hamukuaya et al., 1998; Monteiro et al., 2008; Hutchings et al., 2009; Bachèlery et al., 2016) and the regional climate (Hirst and Hastenrath, 1983; Shannon et al., 1986; Rouault et al., 2003; Lutz et al., 2015). The most striking example is at interannual frequencies, with episodes during which the **S**ea **S**urface **T**emperature (**SST**) remains ~2 °C above or below the seasonal means for ~3–6 consecutive months in the Angolan and NBUS sub-systems. These extreme events are known as Benguela Niños and Niñas (Shannon et al., 1986; Florenchie et al., 2003, 2004). A characteristic portrayal of the SST anomalies during the 2001 Benguela Niños event in the area is given in Fig. 1a. This variability is also associated with substantial modulations of nutrients supply (Bachèlery et al., 2016) and of the oxygen content (Monteiro and van der Plas, 2006; Monteiro et al., 2008, 2011; Bachèlery et al., 2016) during several months, as illustrated on Fig. 1b. The extended duration of non-suitable habitat conditions (hypoxia, lack of food supply) is thought to affect the marine biodiversity and the abundance of the fish stocks (Woodhead et al., 1997a, 1997b, 1998; Hamukuaya et al., 1998; Gammelsrød et al., 1998; Binet et al., 2001; Boyer et al., 2001; Boyer and Hampton, 2001; Monteiro et al., 2008).

It has been shown that the coastal interannual variability in the Angolan and NBUS sub-systems and the Benguela Niño and Niña events are significantly related with the equatorial activity (Lübbecke et al., 2010; Bachèlery et al., 2015, 2016; Imbol Koungue et al., 2017; Tchipalanga et al., 2018). The equatorial forcing is associated with the propagation of eastward **E**quatorial **K**elvin **W**aves (**EKW**) along the equatorial waveguide due to trade wind fluctuation in the western - central part of the basin (Illig et al., 2004). Upon reaching the African continent, a fraction of their energy is transmitted southward and propagates along the African west coast as **C**oastal **T**rapped **W**aves (**CTW**). EKW and CTW can be decomposed into individual modal contributions with distinct vertical structures, phase speeds, and dissipation rates that depend on the ocean stratification and, specifically for CTW, on the cross-shore topography (Cane and Sarachik, 1976, 1977, 1979; Huthnance, 1978; Clarke and Van Gorder, 1986; Brink and Chapman, 1987). Throughout their propagations, these waves induce vertical and horizontal currents fluctuations impinging on the temperature (Bachèlery et al., 2015), the coastal biogeochemical conditions (oxygen, nutrient, primary production; Bachèlery et al., 2016) and, so on, the fish stock (Ostrowski, 2007) along the shelf. Displacements of the thermocline (nutricline and oxycline) in sub-surface are mirrored at the surface by fluctuations of the **S**ea **L**evel **A**nomaly (**SLA**) and the SST anomalies which are energetic enough to be detected from space. Over the 2000–2008 period and based on high-resolution numerical

experiments, Bachèlery et al. (2015, 2016) have shown that the equatorial forcing contributes to ~85% of the SLA, oxygen and nitrate interannual anomalies along the Angolan coast. Yet, using remote-sensed observations along with regional ocean model experiments, evidence of poleward propagating interannual CTW have been only found from the equatorial region down to ~20°S–25°S along the western coast of Africa in the NBUS (Ostrowski et al., 2009; Lübbecke et al., 2010; Bachèlery et al., 2015; Imbol Koungue et al., 2017, 2019).

In addition to the equatorial forcing, the local atmospheric forcing also contributes to the coastal interannual variability in the Angolan, and the BUS (Polo et al., 2008; Richter et al., 2010). At a regional scale, interannual wind events trigger significant variations of the upwelling intensity and mesoscale features, as well as locally-forced poleward propagating CTW (Clarke and Brink, 1985). Recently, Imbol Koungue et al. (2017, 2019) suggested that in the Angolan and NBUS sub-systems, both remote and the local forcings act concomitantly, as part of a large-scale wind pattern, to trigger Benguela Niño and Niña events. Notably, they highlighted the development of zonal wind stress anomalies in the western equatorial Atlantic in phase with coastal meridional wind stress fluctuations along the African coast. In the SBUS, since no evidence of remotely-forced interannual CTW propagation have been documented, wind fluctuations are assumed to be the dominant forcing for the coastal interannual fluctuations of the oceanic properties.

To evaluate the contribution of the remote forcing to the sub-seasonal (2–120 days^{-1}) ocean dynamics, numerous studies based their methodology on the use of the SST or the SLA as a proxy for the total wave signal (Polo et al., 2008; Goubanova et al., 2013). However, recent analyses (Illig et al., 2018a; Illig and Bachèlery, 2019) highlighted the importance of assessing the vertical structure and the propagation characteristics (forcing, amplitude, phase speed, dissipation rate, and wind projection coefficient) of individual CTW modes. This allows for a better estimation of the southernmost latitude at which the CTW imprints on the coastal variability and a better prediction of their impact on ocean dynamics and ecosystem resources. Now, at interannual timescale, despite their significant contribution, the CTW modal characteristics along the south-western African continent have never been documented. The objective of this study is to describe the characteristics of the interannual CTW and their impact on the coastal ocean dynamics in the Angola-Benguela upwelling system, as well as on the phenology of Benguela Niños and Niñas. A particular effort is devoted to the documentation of the impact of equatorially-forced CTW on the SBUS. We also aim at unravelling the contribution of the locally-forced CTW from the equatorially-forced CTW. Given the lack of an adequate observation network in the coastal band, our approach relies on the numerical experimentation with a regional ocean model. Two relatively long (51 years), high-resolution simulations of the south-eastern Atlantic Ocean have been carried out in order to examine the equatorially-forced CTW properties as well as to disentangle the role of the equatorial ocean dynamic from the local forcing in modulating the coastal interannual dynamic. To do so, we benefit from a new methodology that allows extracting CTW amplitude from model outputs (Illig et al., 2018b).

The paper is structured as follows: Section 2 presents the methodologies and introduces the regional model configuration, along with the two sensitivity experiments to the interannual forcing. In the Supporting information, we provide a validation of the most realistic simulation. Section 3 is devoted to the analysis of the model outputs. It documents the effect of the interannual equatorially-forced CTW during their journey on the continental shelf ocean properties. It also presents the evaluation of the CTW characteristics (phase speed, magnitude, forcing) in the south-eastern Atlantic Ocean. Finally, a discussion on the phenology of Benguela Niños and Niñas in regard of extreme CTW events is proposed. The main conclusions and perspectives of this work are drawn in the closing section.

2. Model simulations and methods

The model configuration and the methodologies used to extract the contribution of the EKW in the equatorial Atlantic and CTW along the south-western African coast are detailed in this section. Additional information describing the data used in this study, along with the validation of the model performances are given in the Supporting information (Sections S1 and S2).

2.1. Monthly climatologies and interannual anomalies

In order to isolate the interannual variability, we use the following methodology (Mosquera-Vásquez et al., 2014; Bachèlery et al., 2015). First, the time series are linearly detrended over the 1958–2008 period in order to remove the significant trends that are observed in the region (Monteiro et al., 2008; Rouault et al., 2007, 2009). Then, the sub-seasonal variability is filtered out by computing the monthly averages and smoothing them using on a 1-2-1 running weighted average. Interannual anomalies are estimated by subtracting the monthly climatology which is estimated over 1958–2008 (1993–2008) for model solutions (remotely-sensed observation). Finally, time series are re-interpolated onto a 5-day time axis using cubic splines.

2.2. The regional ocean model configuration

The Adaptive Grid Refinement in Fortran (AGRIF) version 3.1 (Penven et al., 2006; Debreu et al., 2012) of the Regional Ocean Modeling System (ROMS; Shchepetkin and McWilliams, 2005) is used in this study to performed the simulations. ROMS is a three-dimensional, free-surface and split explicit time stepping numerical model that solves the Reynolds-averaged Navier–Stokes equations based on the hydrostatic and Boussinesq assumptions. The model uses finite-difference approximations on a horizontal curvilinear Arakawa C grid and vertical stretched topography-following coordinate system. The vertical mixing of tracers and momentum is done using a K-profile parameterisation scheme (KPP; Large et al., 1994).

The configuration developed for this study is similar to the one of Bachèlery et al. (2015) and Illig et al. (2018b). It has been used by Illig and Bachèlery (2019) to assess the coastal subseasonal dynamic. The grid covers the south-eastern Atlantic Ocean including the equatorial band and the BUS, extending from 7°N to 34°S, and from 10°W to the African coast (Fig. 1a). The horizontal resolution is 1/12°, with 37 sigma vertical levels stretched in the surface layer. The model bathymetry is constructed based on the GEBCO_08 global elevation database at 30 arc-second spatial resolution. The domain is initialised using SODA 5-day averaged outputs (Carton and Giese, 2008; *cf.*, Supporting information S1) on the 3rd of January 1958. Model is then spun-up for 5 years using monthly climatological oceanic lateral boundaries conditions and atmospheric surface forcings (estimated over the 1958–1967 period), before reaching a statistical equilibrium state.

The control run simulation, labelled ROMS-CR, is run over 51 years from 1958 to 2008. Forcing prescribed at the surface and at the open lateral ocean boundaries (West and South) are interannual. Temperature, salinity, sea level, and currents boundary conditions come from the 5-day averages of SODA reanalysis and are integrated using a mixed radiation-nudging scheme (Marchesiello et al., 2001). Bulk formulae (Kondo, 1975) are used to derive the freshwater, turbulent, and momentum fluxes using daily DFS5.2 (Dussin et al., 2014; *cf.* Supporting information S1) surface wind, temperature, and humidity fields and surface heat/water fluxes (longwave and shortwave radiations and precipitation rate). As no river discharges are taken into account in our simulation, model **S**ea **S**urface **S**alinity (**SSS**) is restored to the 5-day SODA SSS. 5-day averages of temperature, salinity, sea level, currents and wind stress outputs are saved. The pressure field is calculated offline using the Thermodynamic Equation Of SeaWater 2010 (TEOS-10) from Gibbs-SeaWater Oceanographic Toolbox

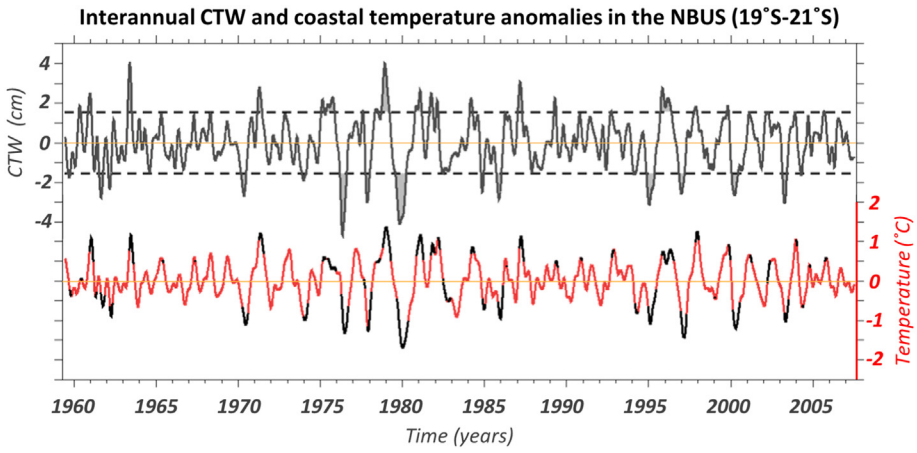

Fig. 2. Time series of ROMS-EQ interannual CTW123 (grey plain line; cm) and temperature (within the first 200 m; bottom red line; °C) anomalies averaged from 19°S to 21°S over a 0.5°-width coastal band. Grey dashed lines and shading denote the position of ± 1.5 STD and the period of major CTW123 events, respectively. The Peak phase of the selected CTW123 events (*cf.* grey shading in the top time series) are reported with black lines on the bottom time series, shifted by ~25 days with CTW123 leading in agreement with the timing found in Fig. 3 (red circle). (For interpretation of the references to colour in this figure legend, the reader is referred to the web version of this article.)

(McDougall et al., 2011).

In the Supporting information S2, we quantify how the model performs as compared to available *in-situ* and satellite observations. This validation exercise reveals a good representation of the equatorial and coastal mean state which controls the vertical structure of the equatorial and coastal waves. The interannual variability is also realistically represented in both sectors. Considering the good performances of the reference simulation ROMS-CR, this model configuration is used to perform a sensitivity experiment labelled ROMS-EQ, to examine the impact of the equatorially-forced CTW propagations on the interannual variability. Assuming some linearities, comparing both simulations will allow for disentangling the contribution of the equatorially-forced CTW to the coastal interannual variability along the south-west coast of Africa from the impact of the local atmospheric forcing.

2.3. Numerical experiment ROMS-EQ

Unlike ROMS-CR, in ROMS-EQ the surface atmospherics forcings (surface wind and heat/water fluxes) prescribed outside of the equatorial band (7°N-10°S) and in the eastern part of the Gulf of Guinea (7°N-10°S/5°E-African continent) are monthly climatologies estimated over the 1958–2008 period. As a result, the interannual variability along the south-western coast of Africa is only triggered by the equatorial dynamics and the internal variability of the model. Note that to avoid discrepancies in the wind stress curl, we have applied a gradual smoothing of the atmospheric forcing fields on a transition band of 2° between the climatological forcing area and regions where the daily atmospheric forcing is prescribed.

2.4. Equatorial Kelvin Wave (EKW) forcing

The EKW forcing is quantified in the equatorial Atlantic over the 1958–2008 period using SODA reanalysis following the methodology used in Illig and Bachèlery (2019) and adapted from Illig et al. (2004). The methodology consists in deriving the vertical structure and phase speed of the three gravest baroclinic modes using time (seasonal and interannual) and zonally slow-varying stratification. Then, pressure and zonal current interannual anomalies are projected onto the baroclinic structures and subsequently onto the meridional structures of the EKW, accounting explicitly for the coastal boundary near the equator in the Gulf of Guinea (Cane and Sarachik, 1979; Illig et al., 2004). EKW are expressed in terms of their contribution to the equatorial **i**nterannual **SLA (iSLA)** averaged within the 1°S-1°N band.

2.5. Coastal trapped waves (CTW) contribution to the coastal variability

Along the south-western African coast, energetics interannual CTW are triggered by the equatorial forcing (EKW) and the alongshore wind stress fluctuations. In order to decipher the impact of both forcings on the CTW dynamics as well as assess the CTW characteristics (amplitude and phase speed), we decomposed the coastal variability of both ROMS experiments into individual CTW modes using the methodology developed by Illig et al. (2018b). First, the cross-shore CTW modal structures and phase speeds (Brink and Chapman, 1987) of the three gravest CTW modes are derived at each latitude along the south-western African continent using ROMS-CR mean (1958–2008) coastal stratification and topography. Then, ROMS-CR and ROMS-EQ CTW mode amplitude are estimated by projecting interannual pressure anomalies onto these structures based on the orthonormal modal structure condition (Brink, 1989). This methodology has shown good skills in estimating sub-seasonal CTW characteristics along the coasts of south-western South-America and Africa (Illig et al., 2018a, 2018b; Illig and Bachèlery, 2019). In this study, CTW are expressed in terms of their contribution to coastal iSLA averaged within the 0.5°-width coastal band.

As most of the energy projects on the three gravest CTW modes (not shown), the CTW propagating signal (CTW123) is considered as the summed-up contribution of the first (CTW1), the second (CTW2) and the third (CTW3) CTW modes, such as:

$$CTW123 = CTW1 + CTW2 + CTW3 \quad (1)$$

2.6. CTW composite analysis

In order to analyse the structure and the amplitude of the interannual anomalies over the continental shelf triggered during CTW propagations, we conducted composite analyses based on CTW123 (*cf.* Section 2.5) events index. The methodology is the following:

i) First, the 1958–2008 reference CTW time series are defined as the interannual anomalies of CTW123 iSLA (*cf.* Eq. (1)) for which the decadal variability is removed by subtracting the 5-year running mean. As an example, the ROMS-EQ CTW123 iSLA is averaged within the coastal band comprised between 19°S and 21°S and displayed on Fig. 2 (grey plain line).
ii) Then, energetic downwelling and upwelling CTW interannual events are defined when CTW123 iSLA magnitude exceeds a given threshold. On Fig. 2, dashed horizontal black lines delineate the ± 1.5 **ST**andard **D**eviation (**STD**) thresholds (used in Section 3.2) and grey shading highlights periods associated with strong CTW propagations.
iii) The delay between the passage of a CTW and its signature on the coastal circulation and water masses is taken into account before performing the composites. Lags are obtained by calculating the maximum lag-correlation between CTW123 and the variable of interest (temperature, SLA, currents components) averaged in a 0.5°

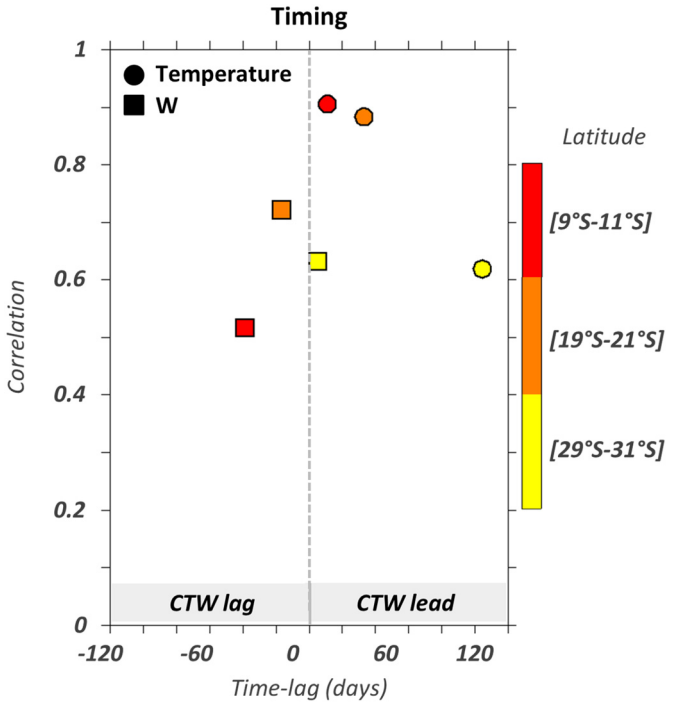

Fig. 3. Timing between the passage of ROMS-EQ interannual CTW and its signature on the coastal ocean properties. Maximum lag-correlation between the interannual ROMS-EQ CTW123 (Eq. (1)) and the coastal (0.5°-width band) temperature (circles) and vertical current (squares) anomalies averaged over the first 200 m and within [9°S–11°S] (red), [19°S–21°S] (orange) and [29°S–31°S] (yellow). Positive lags indicate that CTW leads. (For interpretation of the references to colour in this figure legend, the reader is referred to the web version of this article.)

coastal fringe over the 1958–2008 period. As an example, the lags between the CTW passage and temperature and vertical velocity averaged over the first 200 m are displayed in Fig. 3 for the [9°S–11°S], [19°S–21°S], and [29°S–31°S] domains. Timings between coastal wave peaks and ocean variability will be further discussed in Section 3.4. The red line on Fig. 2 exemplifies the coastal temperature time series averaged within [19°S–21°S] on which the strong CTW propagations have been reported and overlaid with a black line.

iv) The composite is then estimated by averaging the interannual anomalies of the variable of interest during the periods of strong CTW propagations. Note that the decadal variability is primarily filtered out by subtracting the 5-year running mean. Assuming a symmetry between the positive (downwelling) and negative (upwelling) phase of CTW (Florenchie et al., 2004; Bachèlery et al., 2015; Imbol Koungue et al., 2017), interannual anomalies associated with downwelling and upwelling CTW are thus combined together following the methodology of Illig et al. (2014) and Bachèlery et al. (2016). It consists of multiplying by −1 the interannual anomalies during periods of energetic upwelling CTW before averaging all the events together. The obtained composite will thus represent the response of the ocean associated with a strong downwelling CTW propagation.

3. Results

In this section, we analyse the results of the two sensitivity experiments in order to quantify the contribution of the equatorially-forced CTW to the coastal interannual variability in the Angola-Benguela upwelling sub-systems and attempt to track the signature of their propagations along the western African coast from the equator down to the SBUS. We also aim at documenting the characteristics of individual CTW modes namely, their forcing, amplitude, dissipation rate, and

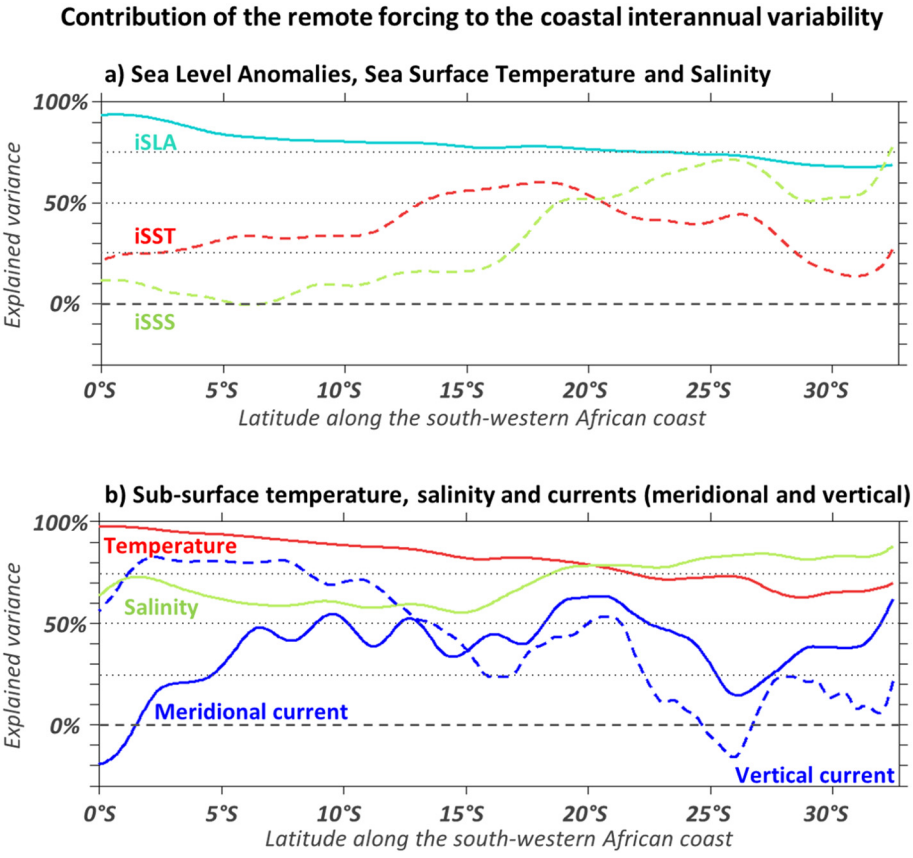

Fig. 4. Explained variance (in %, as defined by Eq. (2)) between ROMS-EQ and ROMS-CR sensitivity experiments, averaged over the 0.5°-width coastal band along south-western Africa. a) **I**nterannual **S**ea **L**evel **A**nomalies (**iSLA**; turquoise line), **S**ea **S**urface **T**emperature (**iSST**; red dashed line) and **S**ea **S**urface **S**alinity (**iSSS**; green dashed line) anomalies. b) Interannual temperature (red line), Salinity (green line), meridional (blue line) and vertical (blue dashed line) currents anomalies averaged over the first 200 m. (For interpretation of the references to colour in this figure legend, the reader is referred to the web version of this article.)

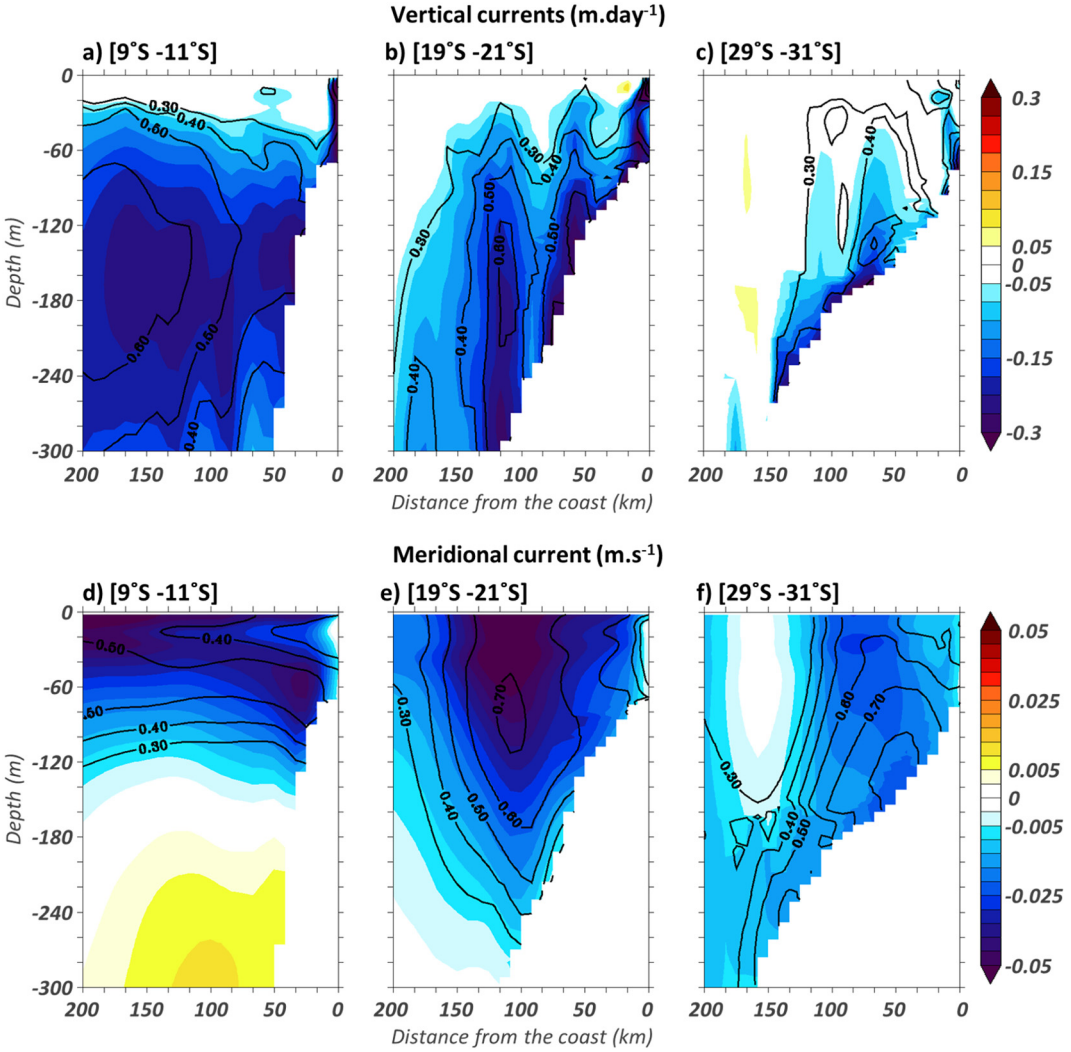

Fig. 5. Composite cross-shore sections at 9°S–11°S (left panels), 19°S–21°S (middle panels), and 29°S–31°S (right panels) of ROMS-EQ interannual vertical (top panels; m.day^{-1}) and meridional (bottom panels; m.s^{-1}) currents anomalies averaged during periods of energetic CTW events (*cf.* grey shading in Fig. 2a). See Section 2.6 for details on the compositing technique. Contours show correlation (1958–2008) between the interannual current variability and CTW123 indexes shifted in time by the corresponding lag obtained in Fig. 3.

phase speed, at interannual timescales.

3.1. Contribution of the equatorial dynamics to the coastal interannual variability

The analysis starts with a comparison between the ROMS-EQ and ROMS-CR model solutions (*cf.*, Sections 2.2 and 2.3). Fig. 4a shows the explained variance between the coastal (0.5° coastal band) interannual variability in the two sensitivity experiments, as a function of the latitude along the south-western African coast. Similar to Eq.1 in Illig et al. (2018a), the explained variance (ExpVar) of ROMS-EQ relative to ROMS-CR is expressed in % and defined as:

$$ExpVar = 100 \times \left(1 - \frac{VARIANCE\,(ROMS_{EQ} - ROMS_{CR})}{VARIANCE\,(ROMS_{CR})}\right) \quad (2)$$

This diagnostic allows for quantifying the amount of the coastal interannual variations in ROMS-EQ, that are in phase and have the same magnitude than the amount of the coastal interannual variability in ROMS-CR, as opposed to the variability triggered by the local atmospheric forcing (surface wind and heat/water fluxes) and the model intrinsic non-linearities. Results show that the coastal iSLA variability induced by the equatorial dynamics in ROMS-EQ is highly coherent with the coastal iSLA fluctuations of ROMS-CR (Fig. 4a; turquoise line). This good coherence, however, decreases with latitude when moving southward, with explained variances along the coasts of Angola (9°S–11°S), Namibia (19°S–21°S) and South Africa (29°S–31°S) equal to ~81%, ~77% and ~70%, respectively. Contrary to the iSLA, interannual **SSS** (**iSSS**) and **SST** (**iSST**) variabilities are only partially explained by the remote forcing. North of 19°S, in the Angolan subsystem, ROMS-EQ explains < 35% of ROMS-CR iSSS anomalies (Fig. 4a; green dashed line). This contribution increases to ~50%–75% in the BUS. Note that ROMS-CR and ROMS-EQ SSS are restored to SODA SSS to compensate for the absence of river runoff in the simulations. The connection with the equatorial variability accounts for < 50% of the coastal iSST variability, except in the Angola-Benguela Area (ABA: ~10°S–20°S) where it peaks to ~60% (Fig. 4a; red dashed line). The ABA is the region where the thermocline breaks to the surface (Florenchie et al., 2004) and Benguela Niño/Niña events are more intense (Fig. 1a).

Previous studies have shown that the impact of CTW on SST is due to fluctuations in the amplitude of the currents and the associated transport of water masses along the continental shelf (Florenchie et al., 2004; Rouault, 2012; Bachèlery et al., 2015; Rouault et al., 2018; Siegfried et al., 2019). However, the signature of CTW is also more

pronounced below the surface near the thermocline where the mean vertical thermal gradient is maximum and where vertical shifts of isotherms induce strong temperature anomalies (Florenchie et al., 2004; Bachèlery et al., 2015). To that extend, the contribution of the equatorial forcing to the subsurface (averaged over the first 200 m) coastal temperature, salinity and currents (meridional and vertical) interannual anomalies is also analysed using the same diagnostic (Fig. 4b). Similar to the iSLA, the sub-surface temperature variability in ROMS-CR has a large fraction (> 70%) explained by ROMS-EQ solutions showing the substantial influence of the equatorial dynamics on the coastal temperature variability in the Angolan, NBUS and SBUS subsystems (red line; Fig. 4b). Similar results are obtained for sub-surface salinity with, nevertheless, a slightly weaker percentage of explained variance ranging from 60% to 90% from the equator to the SBUS (green line; Fig. 4b). The contribution of the equatorial forcing to the current variabilities (meridional and vertical; plain and dashed blue lines on Fig. 4b, respectively) is not as clear as on the iSLA, temperature or salinity variables. This might be partially due to the higher dynamical nature of the currents that immediately respond to ocean and atmospheric perturbation. The equatorial contribution is not continuous from the equator to the SBUS and particularly drops down at Lüderitz (25°S–27°S) and Walvis Bay (16°S–17°S) illustrating the stronger influence of local winds fluctuations on the currents in these two areas (see Section 3.5). Nevertheless, a fair percentage of explained variance of ROMS-EQ relative to ROMS-CR exists: North of 14°S, the coherence between the coastal interannual vertical current anomalies in ROMS-EQ and ROMS-CR remains above ~50% (blue dashed line; Fig. 4b). Within 5°S and 24°S, the remote forcing explains ~40% of the meridional current variability (blue line; Fig. 4b).

3.2. Impact of energetic remotely-forced CTW on the coastal circulation and shelf water masses

As interannual equatorially-forced CTW are identified as the main forcing accounting for the coastal surface and sub-surface interannual variability (Fig. 4), we now document the structure and the amplitude of the interannual anomalies triggered during the passage of remotely-forced CTW on the coastal circulation (Fig. 5) and water masses (temperature and salinity; Fig. 6) along the continental shelf. To do so, we performed a composite analysis (*cf.* Section 2.6) based on the detection of energetic remotely-forced CTW episodes using ROMS-EQ sensitivity experiment outputs. In this experiment, the effects of the interannual local atmospheric forcing have been removed (*cf.* Section 2.3). Focusing on CTW123 iSLA magnitude exceeding 1.5 STD, we identified and combined 41 CTW events including both upwelling (23) and downwelling (18) CTW propagations. The delay between the passage of a CTW and its impact on the coastal variability is taken into account and estimated thanks to a lag-correlation analysis between the CTW123 iSLA and interannual temperature or currents fluctuations. Examples of maximum correlation coefficients and associated time-lags are presented in Fig. 3 for temperature and vertical currents and will be further discussed in Section 3.4. Please refer to Section 2.6 for complete details on the composite methodology.

To begin, we examine the impact of a downwelling CTW on the coastal circulation. Shading in Fig. 5 shows CTW composites of cross-shore sections of the vertical (Fig. 5a, b, c) and meridional currents (Fig. 5d, e, f) interannual anomalies, averaged in three regions along the south-western African coast: [9°S–11°S], [19°S–21°S] and [29°S–31°S], respectively. From the Angolan to the SBUS sub-systems, strong negative vertical and meridional currents anomalies occur along the continental shelf. They illustrate the decrease of the coastal upwelling and of the surface meridional equatorward jet, as well as the intensification of the poleward meridional undercurrent associated with the passage of downwelling CTW. Off the Angolan coast, maximum vertical (meridional) current anomalies of $\sim -0.3\,\mathrm{m.day^{-1}}$ ($\sim -0.05\,\mathrm{m.s^{-1}}$) are located in the sub-surface between 100 m and 200 m depth (in the surface layer above 100 m depth). The more South, the more the impact of interannual CTW on the coastal circulation is confined to the continental shelf in the coastal fringe. This can be attributed to the change in the shape of the coastal bathymetry that controls the shape of the CTW modal structures along the south-west coast of the African continent (Illig et al., 2018a). In the BUS, the gentler continental slope favors nearly barotropic CTW characterised by vertical isopleths over the shelf and slope (Fig. 5c and f), while in the presence of a steeper and deeper bathymetry, CTW have baroclinic isopleths oriented offshore (Fig. 5a and d). Superimposed onto the shading, contours show the correlation coefficient between interannual currents (meridional and vertical) and CTW123 anomalies (shifted by a few days according to the delay between the CTW passage and its signature on the coastal ocean variability; Fig. 3; Section 2.6). The linear relationship between equatorially-forced CTW and the coastal circulation is further confirmed by the high correlation that exceeds 0.5 in the three subsystems. Note also that, for both meridional and vertical currents, the spatial structure of the interannual anomalies and the correlation pattern overlay extremely well. Interestingly, while the amplitude of variability is decreasing southward, in particular when reaching the BUS, the correlation remains constant or slightly increases with latitude.

CTW-associated anomalous meridional and vertical currents significantly affect the transport of water masses through advection processes and therefore imprint the temperature and salinity along the shelf. During the poleward propagation of a downwelling CTW, temperature and salinity fluctuations are triggered by the stronger transport of equatorial warm, salty water southward and the reduction of the cold, fresh subsurface water upward (Fig. 5; Bachèlery et al., 2015). Interannual fluctuations of the tracers (temperature and salinity) are in quadrature with the current anomalies (which corresponds to a delay of ~2 months between signals; Fig. 3).

The amplitude and the structure of the temperature and salinity interannual anomalies associated with downwelling CTW propagations along the south-western African coast are presented in Fig. 6. The structure of the temperature (salinity) interannual anomalies exhibit subsurface maxima near the coast in the first 80 km at ~57 m, ~63 m and ~90 m depth (~141 m, ~75 m and ~97 m depth) at [9°S–11°S], [19°S–21°S] and [29°S–31°S], respectively. For both tracers, the magnitude of the anomalies remains high along the coast of Angola and in the NBUS (temperature: ~1.5 °C; salinity: ~0.06 PSU) but significantly decrease in the SBUS (temperature ~0.6 °C; salinity: ~0.03 PSU). This is most likely due to the decrease of the amplitude of the vertical and meridional temperature and salinity gradients (not shown) in the BUS and the dissipation of the energy of the CTW with latitude cause by bottom friction (Illig et al., 2018b). During their propagations, remotely-forced CTW trigger a substantial shift of the thermocline depth of ~10 m, 15 m and 5 m in the 0.5°-width coastal band at [9°S–11°S], [19°S–21°S] and [29°S–31°S], respectively. Alike Fig. 5, we observe a good coherence between temperature (salinity) and CTW123 interannual variations, with nearshore maximum correlation coefficients of ~0.9, 0.9 and 0.7 (0.8, 0.8 and 0.5) located near the coast within ~140-180 m depth at 9°S–11°S, 19°S–21°S and 29°S–31°S, respectively. In the BUS, correlation patterns follow the slope of the continental shelf. Interestingly, except in the SBUS, the correlation patterns do not coincide with the structure of the cross-shore tracers interannual anomalies (Fig. 6a, b, d, e). Interannual anomalies exhibit maximum values in the subsurface above 100 m depth, under the thermocline at the location of the maximum gradient (not shown). As noted in Bachèlery et al. (2015, 2016), the oceanic response to CTW propagations on temperature and biogeochemical tracers is dominated by the advection processes and then, highly influenced by the mean vertical distribution of the tracers. In the well stratified waters off the coast of Angola, the signature of the CTW is therefore located under the mixed layer where the maximum vertical gradients are located (Fig. 6a and d), while in the well mixed BUS, most of the variations appear along the slope of the continental

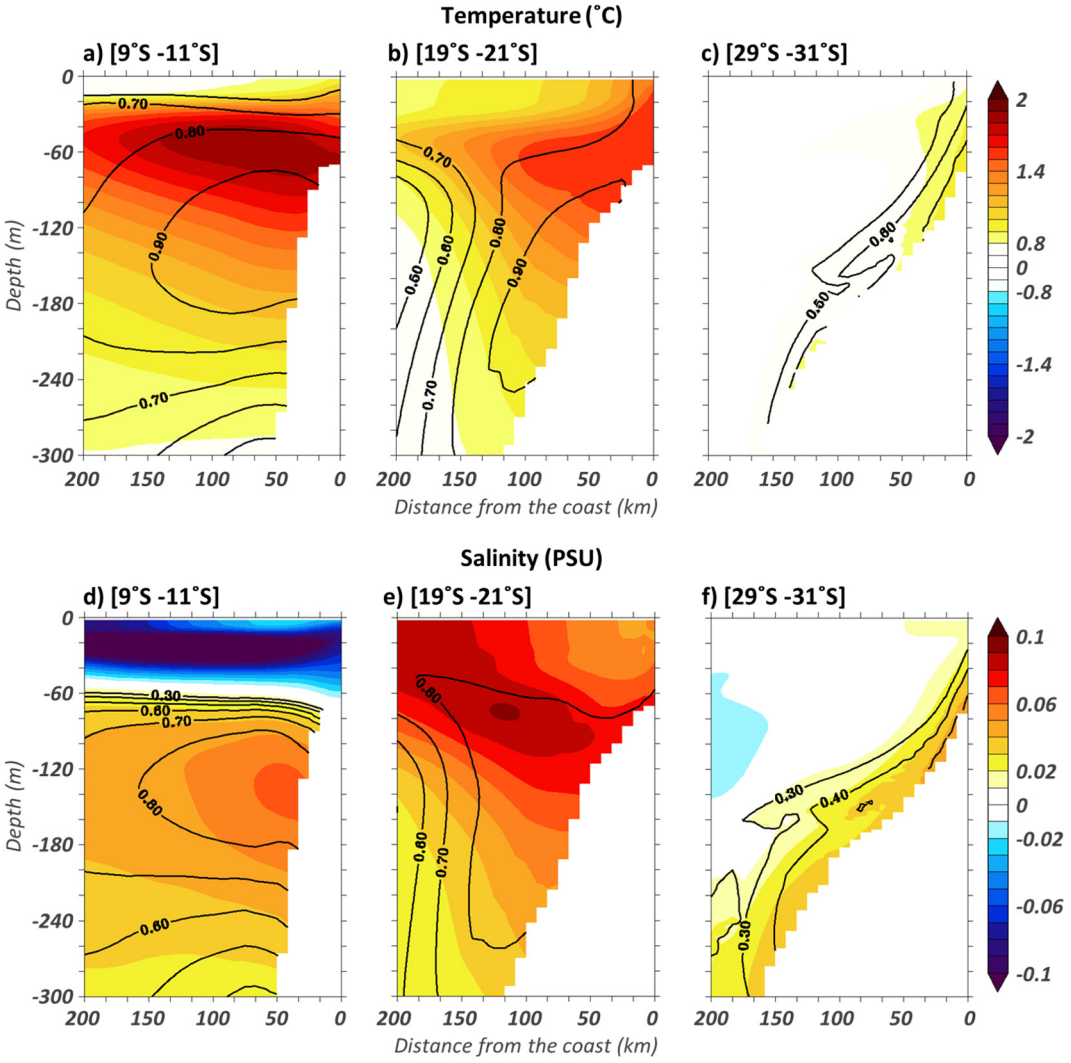

Fig. 6. Same as Fig. 5 for temperature (top panels; °C) and salinity (bottom panels; PSU) interannual anomalies.

shelf in agreement with the barotropic structure of the currents anomalies triggered by CTW (Illig et al., 2018a, 2018b; Fig. 6c and f).

In summary, a substantial part of the coastal interannual variability is driven by the equatorial dynamics. As shown in Fig. 4a, b, > 70% of the iSLA and temperature variability (within the first 200 m) is explained by the propagation of remotely-forced CTW in the SBUS (34°S). This confirms and extends some of the earlier conclusions of Bachèlery et al. (2015), but now for a longer period. It also provides for the first-time strong evidence of the impact of the equatorial dynamics on ocean properties down to the southern tip of south-Africa. If EKW and subsequent propagating poleward CTW are the dominant mechanisms triggering the coastal oceanic variability along the south-western coast of Africa, the associated interannual anomalies are expected to be trackable continuously from the equator to the SBUS. Accordingly, the interannual anomalies at the equator should be significantly correlated with the variability along the coast, allowing a lag to account for the propagation time. The result of this simple diagnostics is illustrated in Fig. 7a using iSLA from AVISO altimetric observations (*cf.* Supporting information S1). As expected, clear propagations associated with significant correlation coefficients and positive increasing lags (white dots on Fig. 7a) are observed down to ~12°S. South from this latitude, the maximum correlation coefficient values significantly decrease and surprisingly, the associated lags start to decrease with latitude toward negative values portraying a concave/banana-shaped pattern. Therefore, according to the patterns presented in Fig. 7a, coastal iSLA fluctuations in the SBUS (~30°S) peak ~20 days before the fluctuations in the Gulf of Guinea at the equator. The decrease of the consistency toward high latitude can be attributed to the resolution of the satellite observations, the lack of data near the coast due to contamination that does not allow accurate detection of the CTW propagations further poleward (Polo et al., 2008; Goubanova et al., 2013). However, we obtain similar patterns with ROMS-CR (Fig. 7b) and ROMS-EQ (Fig. 7c) model solutions. To explain this pattern, we will now further investigate the characteristics (amplitude and phase speed) of the equatorial forcing focussing in particular on the equatorially-forced CTW using ROMS-EQ model outputs.

3.3. Characteristics of the interannual CTW

The amplitude of equatorially-forced CTW is mainly controlled by the amplitude of the equatorial forcing, as well as by the frictional dissipation and the modal energy scattering they experience along their propagation (due to bottom friction). First, we diagnose the contribution of the interannual propagating EKW (*cf.* Section 2.4) to the iSLA variability in the Gulf of Guinea (Fig. 8a). Within [5°W-10°E/1°S-1°N], the summed-up contribution of the 3 gravest interannual EKW modes (EKW123) explains > 60% of the equatorial iSLA variability with a variance of ~1.4 cm^2 (Fig. 8a - grey bar). In agreement with Illig et al. (2004) the equatorial iSLA is dominated by the contribution of EKW2 which explain ~33% of its variability with a variance of 0.8 cm^2

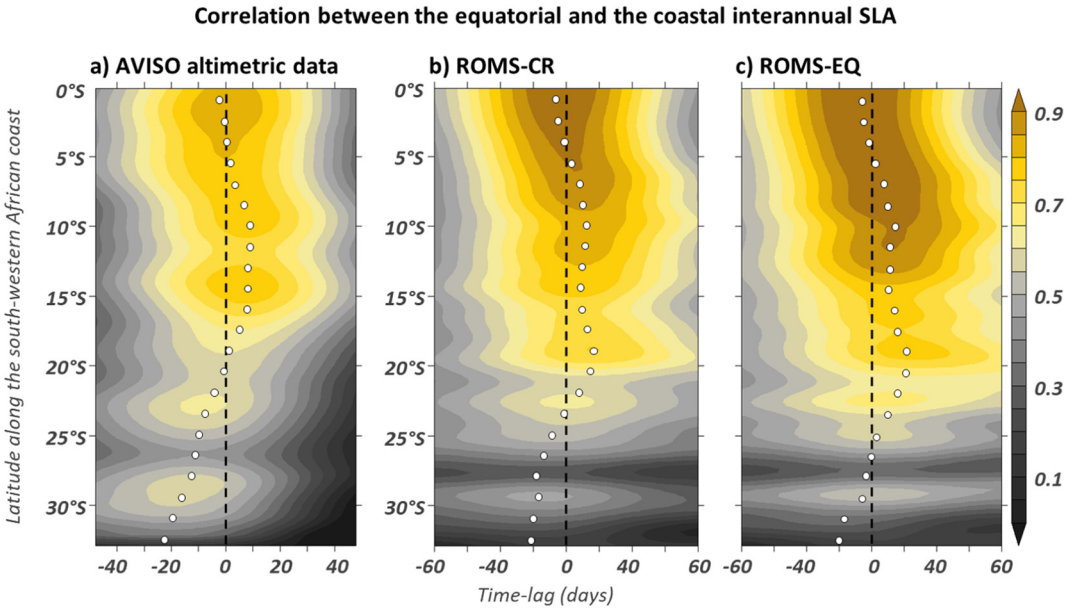

Fig. 7. Lag-correlation between interannual Sea Level Anomalies averaged within [5°W-5°E; 1°S-1°N] and over a 1°-width coastal band as a function of the latitude (y-axis) and lag (x-axis, days). Positive lags correspond to the equatorial variability leading. White dots highlight the timing of the maximum correlation in function of latitude (every 1.5°). a) Remotely-sensed AVISO observations. b) ROMS-CR and c) ROMS-EQ model solutions.

(Fig. 8a - blue bar).

When reaching the African continent, a fraction of the eastward equatorial wave energy is transmitted southward along the west African coast, and the coastal band is, then, considered as an extension of the equatorial waveguide. The evolution of the interannual equatorially-forced CTW activity in function of latitude along the south-western African coasts is presented in Fig. 8 (top numbers in grey bars) by the variance of the ROMS-EQ CTW123 signal. Results reveal a decrease of the amplitude of the CTW123 variability by ~36% (0.9 cm^2) from Angola (7°S–10°S) to South-Africa (28°S–32°S). However, while the CTW123 energy dissipates, its contribution to iSLA remains stable (~70%) or even increases up to ~83% when reaching the SBUS (Fig. 8g). Nearby the equatorial band, down to 18°S, the characteristics of remotely-forced CTW, remains consistent with the remote equatorial forcing. From 7°S–10°S, the coastal iSLA interannual variability is dominated by the contribution of the second CTW modes, with an explained variance of ~49% (Fig. 8b - blue bar). A little further south (11°S–15°S), the contribution of CTW2 tends to decrease, concomitantly with the increase of the contribution of CTW3 (Fig. 8c - blue and green bars). The increasing contribution of CTW3 to iSLA is most likely related to the scattering of CTW2 into CTW3 (Illig et al., 2018b). The higher the mode order, the more dissipative the mode is. Between 15°S and 20°S, the energy of CTW3 drastically decreases, and the less dissipative CTW2 became dominant. Similar to CTW3 and in agreement with the CTW2 frictional dissipation decay, the amplitude of CTW2 starts to drop down from 19°S, and in the BUS, the remotely-forced CTW1 becomes the most energetic process at work. CTW1 accounts for ~68% of the coastal iSLA and ~80% of the CTW123 fluctuations in the SBUS between 28°S and 32°S (Fig. 8g - red bar).

We now look at the propagation pattern of each CTW mode along the south-western African coast. Fig. 9 illustrates the coherence between propagating CTW signal and the coastal iSLA variability along

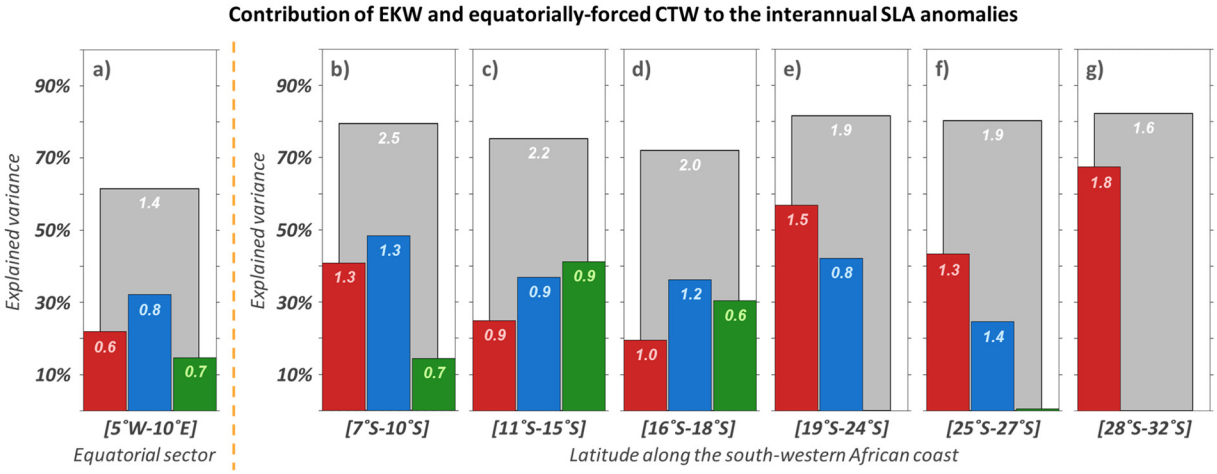

Fig. 8. a) Bar-charts quantify the explained variance (in %; Eq. (2)) of the interannual SODA EKW mode 1 (red), 2 (blue), 3 (green) and their summed-up contribution (grey) to the equatorial ([5°W-5°E;1°S-1°N]) **i**nterannual **S**ea **L**evel **A**nomalies (**iSLA**) of ROMS-EQ. Values on the top bar give the variance (cm^2) of each mode. b–g) Same as panel a) for the ROMS-EQ CTW contributions to the coastal (in a 0.5° width band) iSLA averaged within b) [7°S-10°S], c) [11°S–15°S], d) [16°S–18°S], e) [19°S–24°S], f) [25°S–27°S], and, g) [28°S–32°S]. (For interpretation of the references to colour in this figure legend, the reader is referred to the web version of this article.)

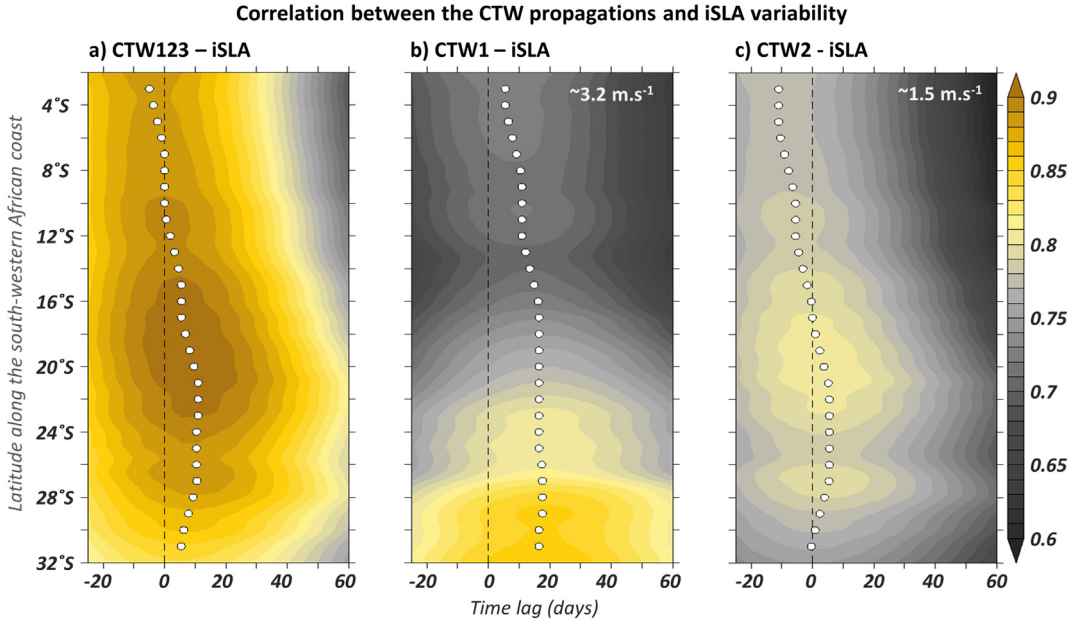

Fig. 9. Lag-correlation between interannual ROMS-EQ CTW signal ((a) summed-up contribution of mode 1, 2 and 3; (b) mode 1; (c) mode 2) averaged within [7°S–9°S - 0.5° coastal band] and the **i**nterannual **S**ea **L**evel **A**nomalies (**iSLA**) as a function of latitude along the south-western coast of Africa (y-axis) and time lag (x-axis, days). Positive lags stand for the CTW signal leading. White dots denote the timing of the maximum correlation in function of latitude (every 1°). Values listed in the right upper corner (in white) correspond to the modal CTW phase speed ($m.s^{-1}$) estimated based on the slope of least-squares best-fit straight lines passing through the maximum correlations (white dots) within [4°S–32°S], and [4°S–22°S] for panel b) and c) respectively.

the south-west coast of Africa using ROMS-EQ model outputs. We compute the lag-correlation between CTW123 or individual CTW modes, averaged within 7°S–9°S at the coast and the coastal iSLA at each latitude. We averaged the interannual CTW contributions within 7°S–9°S at the coast because it corresponds to the theoretical critical latitude (Clarke and Shi, 1991) at which the waves are trapped at the coast (Bachèlery et al., 2015; Illig et al., 2018b). The time-lag allows showing the CTW propagations delay. A positive time-lag means that the CTW signal is leading iSLA anomalies.

First, results show propagating patterns along the south-eastern African coast that are phase-shifted. For instance, near the equator at 8°S, the correlation coefficients between CTW1 (CTW2) and the iSLA are maximum when the CTW signal leads (lags) by ~10 days (Fig. 9b, c).

This is explained by the fact that individual CTW modes propagate at different phase speeds (*i.e.* CTW1: 5.5 $m.s^{-1}$; CTW2: 2.3 $m.s^{-1}$; CTW3: 1.2 $m.s^{-1}$; theoretical phase speed from Illig et al., 2018b). The delay is further accentuated because similar to CTW gravest EKW modes also propagate faster than higher-order modes and reach the west coast of the African continent first. Then, the further south, the more the delay between modes increases.

Results reveal clear poleward propagations of interannual CTW123 (Fig. 9a) along the south-west coast of Africa from 0°S to 23°S with significant maximum correlation (Fig. 9a – white dots) associated with monotonically increasing time-lags when moving southward. Further south, the maximum correlation coefficient decreases, and the associated lags are not increasing with latitude. This propagating pattern resembles the banana-shaped pattern in Fig. 7. The coherence with individual CTW modes (Fig 9b, c), reveals that along the south-western coast of Africa, from 0°S to 23°S, the iSLA variability correlates best with the CTW2. Alike Fig. 9a, south of 23°S, the maximum correlation values diminish, and the associated lags cease to increase linearly (Fig. 9c). Note that, a similar propagating pattern is obtained with CTW3 but with much lower correlation values (< 0.45) and only significant between 12°S and 14°S (not shown). The coherence with CTW1 (along with the time-lags) is, however, quasi continuously increasing with latitude poleward until it reaches a maximum value of ~0.85 in the BUS (south of 23°S; Fig. 9b). The fast weakly dissipative CTW1 impinged the iSLA in the SBUS before the dominant second mode reaches the Angolan and NBUS sub-systems. This results in a significant correlation pattern that departs from a linear path in the BUS and rather take a concave shape. The apparent timing inconsistency (Figs. 7 and 9a) is linked to the change in the dominant CTW mode from the second to the first, south of 23°S.

Finally, using the results of Fig. 9, we further evaluate the averaged phase speed of each CTW mode propagations. Modal CTW propagation velocities are estimated based on the slope of least-squares best-fit straight lines passing through the maximum correlations (white dots in Fig. 9b, c) at each latitude (within the latitudinal domain where their contribution is dominant). Phase speeds obtained are ~3.18 $m.s^{-1}$ and ~1.55 $m.s^{-1}$ for CTW1 (from 4°S to 32°S) and CTW2 (from 4°S to 22°S), respectively. These velocities are in fair agreement with theoretical phase speeds of the interannual CTW modes in the south-eastern Atlantic Ocean (Illig et al., 2018b).

3.4. Timing of CTW on the coastal ocean variability

We now examine the timing between the passage of a CTW and its impact on the coastal currents and temperature variability using ROMS-CR outputs. Similar to Fig. 9a, we perform a lag-correlation analysis between the interannual CTW123 activity averaged within [7°S–9°S] and the coastal (1°-width coastal band) vertical (Fig. 10a) and meridional (Fig. 10b) currents averaged in the [0-200 m depth] surface layer at each latitude along the south-western African coast. Positive time-lags indicate that CTW123 leads the coastal circulation variability. During the passage of a downwelling CTW, vertical and meridional current fluctuations yield a shift in the position of the thermocline mirrored at the surface by fluctuations of the SLA. Therefore, the maximum correlation between the iSLA CTW123 index and the current fluctuations is associated with negative time-lags (Figs. 10a, b and 2). The propagating patterns significantly differs from the one obtained with iSLA (Fig. 9a), with maximum correlations pattern (> 0.5) following a straight path from the equator down to the SBUS. The latter is associated with a significant slower propagation speed of ~0.8 $m.s^{-1}$

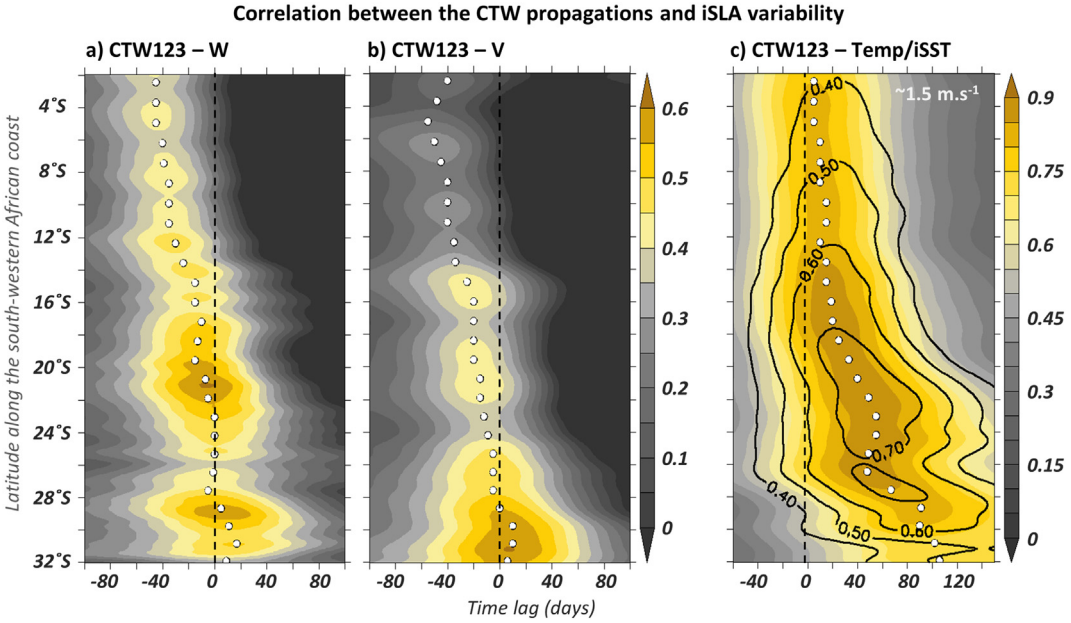

Fig. 10. Lag-correlation between the ROMS-EQ interannual CTW123 signal (averaged within 7°S–9°S - 0.5° coastal band) and **i**nterannual (a) vertical current, (b) meridional current, (c) temperature and **S**ea **S**urface **T**emperature (**iSST**; contours) anomalies as a function of latitude along the south-western coast of Africa (x-axis) and time lag (y-axis, days). Positive lags stand for the CTW signal leading. White dots denote the timing of the maximum correlation in function of latitude (every 1°). The temperature and currents variable have been averaged over the first 200 m depth within a 1° coastal band.

(estimated within [4°S–32°S]) as compared to iSLA propagative pattern (Fig. 9a). The analysis of the impact of interannual CTW propagations on the 0-200 m integrated coastal temperature fluctuations (Fig. 10c, shading) and on the iSST (Fig. 10c, contours) discloses an analogous linear pattern from the equator to ~19°S. Maximum correlations are however higher (> 0.7) and the estimated propagation speed is 1.53 $m.s^{-1}$ (estimated within [4°S–17°S]). In the BUS (19°S–32°S), the alongshore coherency pattern with interannual temperature variability broadens toward larger time-lags and the propagation speed drastically slows down to ~0.3 $m.s^{-1}$ (estimated within [19°S–32°S]). The comparison between Figs. 9a and 10 reveals that the propagative characteristics of the coastal waves are substantially different when analysing oceanic fields that are affected by slow advection processes, as opposed to SLA or thermocline depth interannual variations. Also, the discrepancy between these dynamics seems to depend on the region of interest, with larger differences between iSLA and iSST reported in the BUS. The latter are most likely associated with the specific dynamics and mean state in this major eastern boundary upwelling system, associated with a deeper thermocline, an intense mesoscale activity, and of particular interest is the presence of the equatorward Benguela Jet (Shannon and Nelson, 1996; Shillington, 1998; Shillington et al., 2006) that flows in opposite direction to the poleward CTW propagations. The identification of the processes at work requires more analyses that are beyond the scope of the present paper.

3.5. Role of the local forcing in triggering interannual local CTW

Even if we have shown that the local forcing is not the dominant mechanism behind the coastal interannual variability, atmospheric fluctuations generate local wind-forced CTW propagations. Along the south-west African coast, the alongshore wind stress contains a substantial amount of energy at interannual timescales. The magnitude of the interannual wind fluctuations is displayed in Fig. 11a as a function of latitude along the coast. The variance of the coastal wind stress is found to increase from North to South with lower values (0.005–0.007 $N.m^{-2}$) North of 12°S, in the Angolan subsystem. Also, the magnitude of the interannual wind activity exhibit two clear maxima in the NBUS at Cape Frio (~18°S) and the SBUS at Lüderitz (~26°S) which correspond to the two areas where the smallest equatorial contribution to the coastal vertical current variability have been reported (*cf.* Section 3.1; Fig. 4).

In order to quantify the fraction of the CTW variability explained by the coastal winds, Fig. 11b compares the variance of interannual CTW123 anomalies in ROMS-CR and ROMS-EQ (dark and pale grey shading, respectively) in function of latitude along the south-west African coast. Results show, that, from the equator to the SBUS, there is no striking differences in the amount of energy of the propagating interannual CTW between the two experiments. We quantify a maximum difference in variance smaller than 0.1 cm^2 which represents only ~5% of the magnitude of the interannual ROMS-CR CTW123 anomalies. Furthermore, Fig. 11c shows the good coherence between the remotely-forced CTW123 relative to the ROMS-CR CTW123 (ExpVar in plain grey line) which explains, within the three subsystems, > 75% of the fluctuations. We observe a slightly stronger CTW123 activity in the BUS in ROMS-CR compared to ROMS-EQ (Fig. 11b), concomitantly with the enhance interannual variability of the coastal wind in the same region (Fig. 11a). The response of the ocean to wind stress fluctuations is highly dependent on the ocean stratification which controls how the wind forcing will projects its energy onto the different CTW modes. Between 15°S–30°S (Fig. 11cd in Illig et al., 2018a), where interannual wind stress variability is strong (Fig. 11a), Illig et al. (2018a) have shown that the wind projects preferentially on CTW1. In line with their study, model results show that coastal wind interannual fluctuations in the BUS mainly force interannual CTW1 (Fig. 11c - red plain and dash lines). Indeed, while the impact of local wind stress on each CTW mode between 4°S and 19°S is non-significant, in the BUS (SBUS ~30°S) it accounts for an increase in the amplitude of CTW1 of ~10% (~20%). Wind-forced CTW1 variations in the BUS are not expected to be in phase with remotely-forced variability and might affect the timing and the coherence between the equatorial and the coastal variability. As a result, the link between the equatorial variability and the iSLA in the BUS is slightly weakened when analysing ROMS-CR outputs (not shown) compared to ROMS-EQ (Fig. 9).

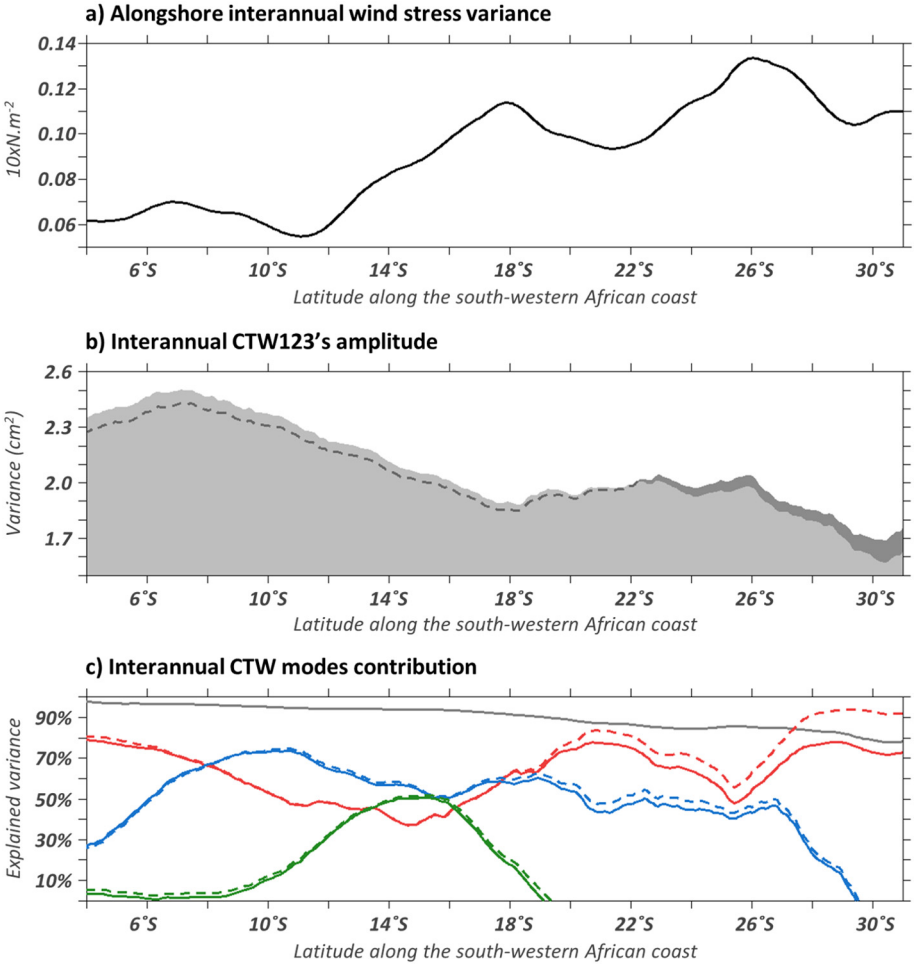

Fig. 11. a) Variance of the interannual alongshore wind stress anomalies ($10 \times N.m^{-2}$) as a function of latitude along the south-western coast of the African continent using ROMS-CR outputs. Wind data have been averaged within a 2°-width coastal band. b–c) Mean (1958–2008) interannual CTW characteristics averaged over a 0.5°-width coastal band. b) Variance of the summed-up contribution of the three gravest CTW modes (CTW123; Eq. (1)) to iSLA (cm) in function of latitude along the south-western African coast. Dark and pale grey show the results for the ROMS-CR and ROMS-EQ, respectively. c) Plain lines account for the explained variance (in %; *cf.* Eq. (2)) of ROMS-EQ CTW modes 1 (red), 2 (blue), 3 (green) and their summed-up contribution (grey) relative to ROMS-CR CTW123. Dash lines show the same quantification for ROMS-CR. (For interpretation of the references to colour in this figure legend, the reader is referred to the web version of this article.)

4. Discussion: Benguela-Angola Niño and Niña analysis

In this study, we have shown that the equatorial forcing, through the propagation of remotely-forced CTW, explains a large amount of the interannual coastal variability and, in particular, it controls 70% of the 0–200 m integrated temperature fluctuations (Sections 3.1 and 3.2). It is now natural to discuss the relation and phasing between energetic CTW and the phenology of the Benguela Niños and Benguela Niñas. We therefore explore the coherence between our CTW123 index and the occurrences of extreme warm and cold events using the most realistic experiment ROMS-CR.

As pointed out by Lübbecke et al. (2010), there is no consensus in the scientific community on a criterion that identifies a Benguela Niño or Niña event. For instance, Florenchie et al. (2004) define an anomalous event when the magnitude of the monthly iSST averaged over the ABA region (10.5°S–19.5°S – 8.5°E–15.5°E) exceeds 1 °C. Lübbecke et al. (2010) consider major events as periods during which iSST fluctuations within ABA are larger than ± 0.7 STD for at least three consecutive months. Imbol Koungue et al. (2017, 2019) classify Benguela Niños and Niñas based on the analysis of the surface temperature in three distinct coastal domains of their interest (10°S–15°S, 15°S–19°S or 19°S–24°S). Extreme (moderate) events are identified when their indexes exceed a ± 1 STD threshold for 3 (2) consecutive months. The most complex definition is found in Lutz et al. (2013), with the objective to connect the coastal SST variability to an equatorial index. These criteria all have in common that they examine the temperature variations in the surface layer. Yet, it has been shown by Florenchie et al. (2004) and Bachèlery et al. (2015) and supported by our results that the maximum temperature variability is located under the mixed-layer, approximately at the mean depth of the thermocline. In line with the aforementioned studies, we define here and compare two criteria for classifying Benguela Niño/Niña events and investigate their relationship with extreme CTW events. Both our criteria are defined when coastal (1°-width coastal band) interannual temperature anomalies averaged within [10°S–20°S] remain higher than ± 1 STD for at least 3 months in a row. The first criteria (CRIT-SURF) considers the temperature averaged in the surface layer (within the first 20-meter depth), while the second one (CRIT-SUBS) uses the temperature fluctuations below the mixed layer (averaged [within 50-60 m] depth). The ABA region undergoes a substantial decadal variability (Hutchings et al., 2009; Moloney et al., 2013) that results in long periods of warm or cold conditions, over which the interannual anomalies are superimposed. To focus exclusively on the interannual variations (period ~18 months; Florenchie et al., 2004; Bachèlery et al., 2015), prior to the methodology described above, we removed the lower-frequency component by subtracting the 5-year running mean. Therefore, the timing (start/end), duration, and amplitude of identified events can differ from other studies, as discussed in Imbol Koungue et al. (2019).

Fig. 12a displays the iSST time series along with the identified Benguela Niño/Niña episodes (yellow and turquoise stars, respectively) based on CRIT-SURF methodology. A total of 31 events (17 warm and 14 cold events) are selected over the 1958–2008 periods. Most of these events have been documented in the literature, including the extreme warm events in 1960–1961 (Imbol Koungue et al., 2019), 1963 (Shannon et al., 1986; Lutz et al., 2013), 1984 (Shannon et al., 1986; Florenchie et al., 2003; Rouault et al., 2003; Rouault, 2012), 1995 (Gammelsrød et al., 1998), 1999 (Mohrholz et al., 2001), and 2001 (Rouault et al., 2007) and the cold events in 1983 (Florenchie et al.,

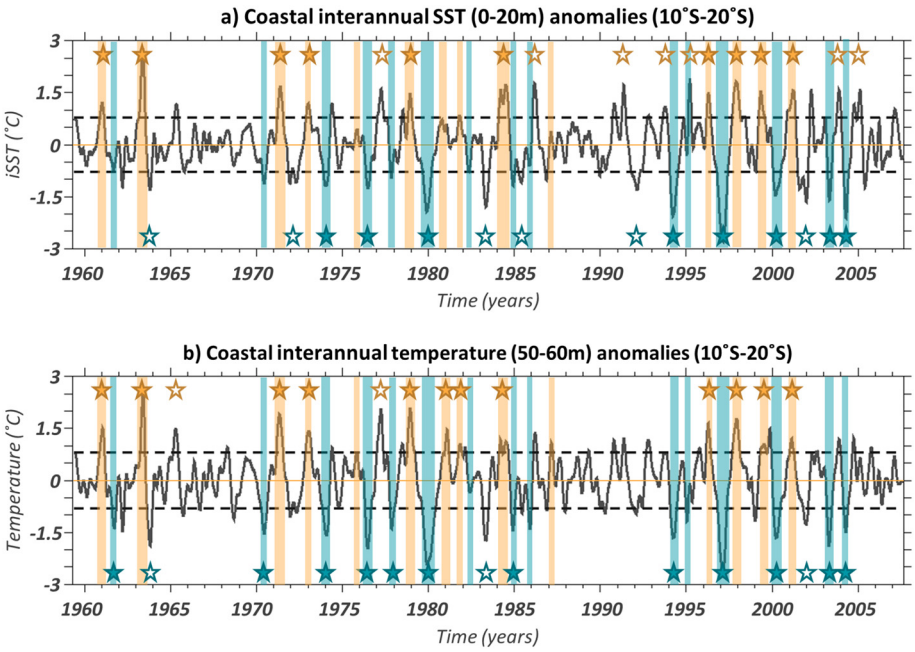

Fig. 12. a) ROMS-CR 0–20 m depth **i**nterannual **S**ea **S**urface **T**emperature (**iSST**; °C) anomalies averaged from 10°S to 20°S in an 1°-width coastal fringe. Extreme downwelling and upwelling CTW123 propagating episodes in ROMS-CR (*cf.* Section 2.6 for more details on the threshold) are emphasized with the yellow and turquoise vertical bars, respectively. Yellow (turquoise) stars denote the extreme Benguela Niño (Niña) episodes defined as **iSST** larger than ± 1 STD (grey dashed lines) for at least 3 months. Extreme Benguela Niño (Niña) events that do not coincide with extreme downwelling (upwelling) CTW episodes are depicted by empty yellow (turquoise) stars. b) Same as Fig. 12a for interannual temperature anomalies averaged under the mixed layer between 50 and 60 m depth. (For interpretation of the references to colour in this figure legend, the reader is referred to the web version of this article.)

2004), 1985, 1992 (Imbol Koungue et al., 2019), 1997 (Florenchie et al., 2004), and 2003 (Bachèlery et al., 2015). Periods of strong downwelling and upwelling CTW events (vertical yellow and turquoise bars) are overlaid on Fig. 12a. For consistency, here CTW events are considered extreme when the time series of the summed-up contribution of the 3 first CTW modes to coastal iSLA (CTW123) averaged within [10°S–20°S] exceeds ± 1 STD for 3 months in a row. Results show that there is a good correspondence between indexes: of the 31 Benguela Niño/Niña events, 18 events (10 warm (yellow-filled stars; Fig. 12a) and 8 cold (turquoise-filled stars; Fig. 12a)) are in phase with peaks in the CTW123 index, *i.e.* 59% of the events. Among the 13 events that do not strictly coincide, 4 are, nevertheless, in phase with only moderate CTW123 activity (defined as CTW123 exceeding ± 1 STD for 2 months). Moreover, when analysing the contribution of individual CTW mode, results reveal that these events are concomitant with the propagation of strong CTW3 (not shown), whose contribution is counterweighted by CTW1 and CTW2. As a result, 22 (18 + 4) events can be related to CTW propagation, which increase the detection performances to 71% of the temperature events. This yet again emphasises the importance of disentangling the contribution of individual CTW modes to better understand the dynamics of the extreme events in the Angola-Benguela upwelling system. The same analysis but using the subsurface temperature criterion (CRIT-SUBS), is presented in Fig. 12b. Interestingly, the agreement between both signals becomes stronger when considering the index in sub-surface: only 5 events (3 cold (1963, 1983, and 2001–2002) and 2 warm (1965 and 1977)) out of a total of 29 extreme events selected here are not associated with intense CTW123 episodes. This represents a total of 83% of coherence (not shown) between signals. As alluded to earlier, these specific 5 events are in phase with moderate CTW123 activity and in particular, strong CTW3 propagations (not shown). Hence, 100% of the extreme temperature conditions below the mixed layer can be related to energetic CTW propagations. This remarkable correspondence (71% in surface and 100% in subsurface) confirmed the high dynamical connection between CTW and extreme temperature conditions along the continental shelf. Benguela Niños and Niñas are associated with fluctuations in the oxygen content of the shelf water (Fig. 1b; Monteiro and van der Plas, 2006; Monteiro et al., 2008, 2011) and significantly affect the marine ecosystem and fish resources (Binet et al., 2001; Gammelsrød et al., 1998). Therefore, it is likely that extreme low-oxygen episodes along the continental shelf and their ecological consequences are connected to CTW propagations. The advent of satellites made it possible to document Benguela Niños and Niñas events as it provides surface observations on a wide spatial and temporal coverage. However, our results suggest that the understanding of the phenology of hypoxic and Benguela Niños and Niñas events, can be significantly improved when also documenting and analysing the sub-surface variability. This will, for instance, require the implementation of mooring monitoring on the shelf where the CTW signature is substantial, similar to the PIRATA observational network in the tropical Atlantic.

The analysis of Fig. 12 reveals some differences in the classification of the extreme events between the surface and the sub-surface. In fact, 9 of the Benguela Niño and Niña events (warm: 1986, 1991, 1993, 1995, 2003, 2005; cold: 1972, 1985, 1992; yellow and turquoise empty stars, respectively) only occur at the surface (Fig. 12a), not fulfilling the CRIT-SUBS criterion (Fig. 12b). Most of them nonetheless, coincide with moderate temperature events in sub-surface (Fig. 12b) and moderate CTW propagations (not shown). This implies that the local atmospherics forcing may enhance the amplitude of the extreme temperature episodes in surface mixed layer (Florenchie et al., 2004; Lübbecke et al., 2010; Richter et al., 2010; Bachèlery et al., 2015; Imbol Koungue et al., 2019). This is in line with the recent study of Imbol Koungue et al. (2019) which highlights the concomitant role of both, the equatorial and the local forcing, as part of a large-scale wind anomaly pattern over the South Atlantic Ocean, in triggering Benguela Niños/Niñas.

However, our results reveal also cases where the atmospheric forcing (through CTW generation, upwelling and evaporation processes) conceal the signature of the remotely-forced CTW in the surface layer. This is in particular the case for the sub-surface 1965, 1981 warm (1961, 1977, 1984 cold) events (Fig. 12b) which are associated with strong CTW123 propagations but do not fulfil the CRIT-SURF criterion (Fig. 12a). For instance, a few months before the development of the extreme warm 1995 event, the propagation of a strong upwelling CTW occur along the south-western African coast (Fig. 12 - blue bars), which effects (uplifting of the thermocline and cold temperature anomalies) are recorded in the sub-surface temperature (Fig. 12b). Surprisingly, in the surface layer, the temperature fluctuations (Fig. 12a) portray a positive anomaly consistent with the 1995 Benguela Niño (Gammelsrød et al., 1998). Our results therefore support the finding of Richter et al. (2010) who disassociated the development of this event to the equatorial forcing. However, using composites of Benguela Niño events over

the 1958–2000 period, Lübbecke et al. (2010) did not find stronger wind stress anomalies associated to the development of extreme event. To our knowledge, only the 2016 Benguela Niño event was not predominantly connected to the equatorial dynamics (Lübbecke et al., 2018) but was triggered by local mechanisms associated with wind relaxation and enhanced freshwater from precipitation and river discharges.

5. Conclusion and perspectives

The 1958–2008 coastal interannual variability in the south-eastern Atlantic Ocean is studied using the solutions of two regional ocean model experiments. Our results highlight the strong contribution of the equatorially-forced CTW to the coastal variability along the shelf. For the first time, we were able to track equatorially-forced CTW propagations from the equator down to 34°S in the SBUS where they contribute up to 70% of the interannual SLA, temperature and salinity variability. The decomposition of model coastal variability into CTW contribution allows us to document the effect of energetic CTW propagations on the nearshore oceanic conditions and circulation. In the BUS, interannual remotely-forced CTW induce strong meridional and vertical currents anomalies, maximum in the first 200 m, along the slope of the continental shelf consistent with the nearly barotropic CTW structures. The modulation of currents in turn affects the distribution of temperature and salinity along the continental shelf. The analysis of the characteristics of individual CTW modes reveals that from the equator to 22°S, the coastal variability is controlled by the contribution of the slow propagating and more dissipative second and third CTW modes. Southward, their contribution decreases and the less dissipative CTW1 becomes dominant. As the latter travel faster, its signature on the coastal variability in the SBUS takes place 10 days before the higher modes impinged the NBUS.

Then the dynamical connection between energetics CTW and Benguela Niño/Niña events are evaluated. Our results highlight the remarkably high coherence (71%) between signals. This quantification reaches 100% when: (1) focussing on fluctuations under the mixed layer where the temperature variability is less influenced by the local atmospheric forcing and (2) disentangling the individual CTW modal contribution to the coastal variability.

Finally, our results also suggest a low-frequency (decadal) modulation in the intensity of the surface and sub-surface temperature interannual variability and the frequency of occurrence of warm/cold extreme events (stars on Fig. 12). We denote two periods of strong activity during the [~1975–1985] and [~1995–2005] decades, interspersed with periods of lower interannual variations ([~1962–1970] and [~1985–1994]). These periods are concomitant with changes in magnitude of the CTW activity (vertical bars). Evaluating the mechanisms that control the low-frequency modulation of the coastal interannual variability will be the topic of our next research efforts.

Acknowledgement

This work was supported by the NRF SARCHI chair on “modeling ocean-atmosphere-land interactions”, the Nansen Tutu Centre and the EU H2020 TRIATLAS project under the grant agreement 817578. Model simulations were computed using the CORE supercomputers provided by the CSAG computing facility. The ROMS model simulations were built using the ROMS_TOOLS package (Penven et al., 2006) version 3.1. ROMS can be downloaded from https://www.croco-ocean.org. The authors wish to acknowledge for the use of the Ferret program for analysis and graphics in this paper. Ferret is a product of NOAA's Pacific Marine Environmental Laboratory (Information is available at http://ferret.pmel.noaa.gov/Ferret/). All data used in this study (for model forcing and validation: PIRATA observations, Nansen cruise, AVISO Altimetric data, GlobCurrent estimations, SODA and DRAKKAR forcing products) are publicly available, and detailed information are provided in the Supporting information (Section S1). NOAA, NASA, PANGAEA, CMEMS, GlobCurrent, and Texas A&M University are thanked for development and/or the distribution of these data sets.

Declaration of competing interest

The authors declare no competing interests.

Appendix A. Supplementary data

Supplementary data to this article can be found online at https://doi.org/10.1016/j.jmarsys.2019.103262.

References

Agenbag, J.J., Shannon, L.V., 1988. A suggested physical explanation for the existence of a biological boundary at 24°30′S in the Benguela system. South Afr. J. Mar. Sci. 6, 119–132. https://doi.org/10.2989/025776188784480726.

Bachèlery, M.-L., Illig, S., Dadou, I., 2015. Interannual variability in the South-East Atlantic Ocean, focusing on the Benguela Upwelling System: remote versus local forcing. J Geophys Res Oceans 121, 284–310. https://doi.org/10.1002/2015JC011168.

Bachèlery, M.-L., Illig, S., Dadou, I., 2016. Forcings of nutrient, oxygen, and primary production interannual variability in the southeast Atlantic Ocean. Geophys Res Lett 43. In: 2016GL070288, https://doi.org/10.1002/2016GL070288.

Berrit, G.R., 1976. Les eaux froides côtières du Gabon à l'Angola sont-elles dues à un upwelling d'Ekman? Cah. ORSTOMSérie Océan. 14, 273–278.

Binet, D., Gobert, B., Maloueki, L., 2001. El Niño-like warm events in the Eastern Atlantic (6N, 20S) and fish availability from Congo to Angola (1964–1999). Aquat. Living Resour. 14, 99–113. https://doi.org/10.1016/S0990-7440(01)01105-6.

Boyer, D.C., Hampton, I., 2001. An overview of the living marine resources of Namibia. South. Afr. J. Mar. Sci. 23, 5–35. https://doi.org/10.2989/025776101784528953.

Boyer, D., Cole, J., Bartholomae, C., 2000. Southwestern Africa: Northern Benguela Current Region. Mar. Pollut. Bull. Seas at the Millennium: an Environmental Evaluation 41, 123–140. https://doi.org/10.1016/S0025-326X(00)00106-5.

Boyer, D.C., Boyer, H.J., Fossen, I., Kreiner, A., 2001. Changes in abundance of the northern Benguela sardine stock during the decade 1990–2000, with comments on the relative importance of fishing and the environment. South. Afr. J. Mar. Sci. 23, 67–84. https://doi.org/10.2989/025776101784528854.

Brink, K.H., 1989. Energy conservation in coastal-trapped wave calculations. J. Phys. Oceanogr. 19, 1011–1016.

Brink, K.H., Chapman, D.C., 1987. Program for computing properties of coastal-trapped waves and wind-driven motions over the continental shelf and slope. Woods Hole Oceanogr. Inst., Tech. Rep. WHOI-87-24.

Cane, M., Sarachik, E., 1976. Forced baroclinic ocean motions. 1. Linear equatorial unbounded case. J Mar Res 34, 629–665.

Cane, M., Sarachik, E., 1977. Forced baroclinic ocean motions. II- The linear equatorial bounded case. J. Mar. Res. 35.

Cane, M., Sarachik, E., 1979. Forced baroclinic ocean motions. 3. Linear equatorial basin case. J Mar Res 37, 355–398.

Carr, M.-E., Kearns, E.J., 2003. Production regimes in four Eastern Boundary Current systems. Deep Sea Res. Part II Top. Stud. Oceanogr. The US JGOFS Synthesis and Modeling Project: Phase II 50, 3199–3221. https://doi.org/10.1016/j.dsr2.2003.07.015.

Carton, J.A., Giese, B.S., 2008. A reanalysis of ocean climate using Simple Ocean Data Assimilation (SODA). Mon Wea Rev 136, 2999–3017. https://doi.org/10.1175/2007MWR1978.1.

Chavez, F.P., Messié, M., 2009. A comparison of Eastern Boundary Upwelling Ecosystems. Prog. Oceanogr., Eastern Boundary Upwelling Ecosystems: Integrative and Comparative Approaches: Integrative and Comparative Approaches, 2–8 June 2008, Las Palmas, Gran Canaria. Spain Eastern Boundary Upwelling Ecosystems Symposium 83, 80–96. https://doi.org/10.1016/j.pocean.2009.07.032.

Clarke, A.J., Brink, K.H., 1985. The response of stratified, frictional flow of shelf and slope waters to fluctuating large-scale, low-frequency wind forcing. J. Phys. Oceanogr. 15, 439–453. https://doi.org/10.1175/1520-0485(1985)015<0439:TROSFF>2.0.CO;2.

Clarke, A.J., Shi, C., 1991. Critical frequencies at ocean boundaries. J. Geophys. Res. 96, 10731–10738. https://doi.org/10.1029/91JC00933.

Clarke, A.J., Van Gorder, S., 1986. A method for estimating wind-driven frictional, time-dependent, stratified shelf and slope water flow. J. Phys. Oceanogr. 16, 1013–1028. https://doi.org/10.1175/1520-0485(1986)016<1013:AMFEWD>2.0.CO;2.

Debreu, L., Marchesiello, P., Penven, P., Cambon, G., 2012. Two-way nesting in split-explicit ocean models: algorithms, implementation and validation. Ocean Model 49–50, 1–21. https://doi.org/10.1016/j.ocemod.2012.03.003.

Dias, C.A., 1983a. Note on the evidence of a permanent southward flow of the upper oceanic tropospheric waters off Angola at 12°S. Collection of Scientific Papers of the International Commission for the Southeast Atlantic Fisheries. Collect. Sci. Pap. Int. Comm. Southeast Atl. Fish. 10, 99–102.

Dias, C.A., 1983b. Preliminary report on the physical oceanography off southern Angola, March and July 1971. Collect. Sci. Pap. Int. Comm. Southeast Atl. Fish. 10, 103–116.

Duncombe-Rae, C., 2005. A demonstration of the hydrographic partition of the Benguela upwelling ecosystem at 26.4S. South. Afr. J. Mar. Sci. 27, 617–628.

Dussin, R., Barnie, B., Brodeau, L., 2014. The Making of Drakkar Forcing Set DFS5.
FAO, 2011. Fisheries & Aquaculture - The Republic of Angola [WWW Document]. URL http://www.fao.org/fishery/facp/AGO/en (accessed 3.19.19).
Florenchie, P., Lutjeharms, J.R.E., Reason, C.J.C., Masson, S., Rouault, M., 2003. The source of Benguela Niños in the South Atlantic Ocean. Geophys. Res. Lett. 30, 1505. https://doi.org/10.1029/2003GL017172.
Florenchie, P., Reason, C.J.C., Lutjeharms, J.R.E., Rouault, M., Roy, C., Masson, S., 2004. Evolution of interannual warm and cold events in the Southeast Atlantic Ocean. J. Clim. 17, 2318–2334. https://doi.org/10.1175/1520-0442(2004)017<2318:EOIWAC>2.0.CO;2.
Gammelsrød, T., Bartholomae, C.H., Boyer, D.C., Filipe, V.L.L., O'Toole, M.J., 1998. Intrusion of warm surface water along the Angolan-Namibian coast in February–March 1995: the 1995 Benguela Nino. South. Afr. J. Mar. Sci. 19, 41–56. https://doi.org/10.2989/025776198784126719.
Goubanova, K., Illig, S., Machu, E., Garçon, V., Dewitte, B., 2013. SST subseasonal variability in the central Benguela upwelling system as inferred from satellite observations (1999–2009). J Geophys Res Oceans 118, 4092–4110. https://doi.org/10.1002/jgrc.20287.
Hamukuaya, H., O'Toole, M.J., Woodhead, P.M.J., 1998. Observations of severe hypoxia and offshore displacement of Cape hake over the Namibian shelf in 1994. South. Afr. J. Mar. Sci. 19, 57–59. https://doi.org/10.2989/025776198784126809.
Hellerman, S., 1980. Charts of the variability of the wind stress over the tropical Atlantic. In: Siedler, G., Woods, J.D., Düing, W. (Eds.), Oceanography and Surface Layer Meteorology in the B/C Scale. Pergamon, pp. 63–75. https://doi.org/10.1016/B978-1-4832-8366-1.50022-4.
Hirst, A.C., Hastenrath, S., 1983. Atmosphere-Ocean mechanisms of climate anomalies in the Angola-tropical Atlantic sector. J Phys Ocean. 13, 1146–1157. https://doi.org/10.1175/1520-0485(1983)013<1146:AOMOCA>2.0.CO;2.
Hutchings, L., van der Lingen, C.D., Shannon, L.J., Crawford, R.J.M., Verheye, H.M.S., Bartholomae, C.H., van der Plas, A.K., Louw, D., Kreiner, A., Ostrowski, M., Fidel, Q., Barlow, R.G., Lamont, T., Coetzee, J., Shillington, F., Veitch, J., Currie, J.C., Monteiro, P.M.S., 2009. The Benguela Current: an ecosystem of four components. Prog. Oceanogr., Eastern Boundary Upwelling Ecosystems: Integrative and Comparative Approaches: Integrative and comparative approaches, 2–8 June 2008, Las Palmas, Gran Canaria, Spain Eastern Boundary Upwelling Ecosystems Symposium 83, 15–32. https://doi.org/10.1016/j.pocean.2009.07.046.
Huthnance, J.M., 1978. On coastal trapped waves: analysis and numerical calculation by inverse iteration. J Phys Ocean. 8, 74–92. https://doi.org/10.1175/1520-0485(1978)008<0074:OCTWAA>2.0.CO;2.
Illig, S., Bachèlery, M.-L., 2019. Propagation of subseasonal equatorially-forced coastal trapped waves down to the Benguela Upwelling System. Sci. Rep. 9, 5306. https://doi.org/10.1038/s41598-019-41847-1.
Illig, S., Dewitte, B., Ayoub, N., du Penhoat, Y., Reverdin, G., De Mey, P., Bonjean, F., Lagerloef, G.S.E., 2004. Interannual long equatorial waves in the tropical Atlantic from a high-resolution ocean general circulation model experiment in 1981–2000. J. Geophys. Res. 109, C02022. https://doi.org/10.1029/2003JC001771.
Illig, S., Dewitte, B., Goubanova, K., Cambon, G., Boucharel, J., Monetti, F., Romero, C., Purca, S., Flores, R., 2014. Forcing mechanisms of intraseasonal SST variability off central Peru in 2000–2008. J Geophys Res Oceans 119, 3548–3573. https://doi.org/10.1002/2013JC009779.
Illig, S., Bachèlery, M.-L., Cadier, E., 2018a. Subseasonal coastal-trapped wave propagations in the Southeastern Pacific and Atlantic Oceans: 2. Wave characteristics and connection with the equatorial variability. J. Geophys. Res. Oceans 123, 3942–3961. https://doi.org/10.1029/2017JC013540.
Illig, S., Cadier, E., Bachèlery, M.-L., Kersalé, M., 2018b. Subseasonal coastal-trapped wave propagations in the Southeastern Pacific and Atlantic Oceans: 1. A new approach to estimate wave amplitude. J. Geophys. Res. Oceans 123, 3915–3941. https://doi.org/10.1029/2017JC013539.
Imbol Koungue, R.A., Illig, S., Rouault, M., 2017. Role of interannual Kelvin wave propagations in the equatorial Atlantic on the Angola Benguela Current system. J. Geophys. Res. Oceans 122, 4685–4703. https://doi.org/10.1002/2016JC012463.
Imbol Koungue, R.A., Rouault, M., Illig, S., Rouault, M., Brandt, P., Jouanno, J., 2019. Benguela Niños and Benguela Niñas in forced ocean simulation from 1958 to 2015. J. Geophys. Res. 124, 5923–5951. https://doi.org/10.1029/2019JC015013.
Kondo, J., 1975. Air-sea bulk transfer coefficients in diabatic conditions. Bound.-Layer Meteorol. 9, 91–112. https://doi.org/10.1007/BF00232256.
Kopte, R., Brandt, P., Dengler, M., Tchipalanga, P.C.M., Macuéria, M., Ostrowski, M., 2017. The Angola Current: flow and hydrographic characteristics as observed at 11°S. J. Geophys. Res. Oceans 122, 1177–1189. https://doi.org/10.1002/2016JC012374.
Lachkar, Z., Gruber, N., 2012. A comparative study of biological production in eastern boundary upwelling systems using an artificial neural network. Biogeosciences 9, 293–308. https://doi.org/10.5194/bg-9-293-2012.
Large, W.G., McWilliams, J.C., Doney, S.C., 1994. Oceanic vertical mixing: a review and a model with a nonlocal boundary layer parameterization. Rev. Geophys. 32, 363–403. https://doi.org/10.1029/94RG01872.
Lett, C., Veitch, J., Lingen, C.D. van der, Hutchings, L., 2007. Assessment of an environmental barrier to transport of ichthyoplankton from the southern to the northern Benguela ecosystems. Mar. Ecol. Prog. Ser. 347, 247–259. https://doi.org/10.3354/meps06982.
van der Lingen, C.D., Shannon, L.J., Cury, P., Kreiner, A., Moloney, C.L., Roux, J.-P., Vaz-Velho, F., 2006. 8 Resource and ecosystem variability, including regime shifts, in the Benguela Current System, in: Shannon, V., Hempel, G., Malanotte-Rizzoli, P., Moloney, C., Woods, J. (Eds.), Large Marine Ecosystems, Benguela. Elsevier, pp. 147–184. https://doi.org/10.1016/S1570-0461(06)80013-3.
Lübbecke, J.F., Böning, C.W., Keenlyside, N.S., Xie, S.-P., 2010. On the connection between Benguela and equatorial Atlantic Niños and the role of the South Atlantic Anticyclone. J. Geophys. Res. 115, C09015. https://doi.org/10.1029/2009JC005964.
Lübbecke, J.F., Brandt, P., Dengler, M., Kopte, R., Lüdke, J., Richter, I., Sena Martins, M., Tchipalanga, P.C.M., 2018. Causes and evolution of the southeastern tropical Atlantic warm event in early 2016. Clim. Dyn. https://doi.org/10.1007/s00382-018-4582-8.
Lutjeharms, J.R.E., Meeuwis, J.M., 1987. The extent and variability of South-East Atlantic upwelling. South. Afr. J. Mar. Sci. 5, 51–62. https://doi.org/10.2989/025776187784522621.
Lutz, K., Rathmann, J., Jacobeit, J., 2013. Classification of warm and cold water events in the eastern tropical Atlantic Ocean. Atmospheric Sci. Lett. 14, 102–106. https://doi.org/10.1002/asl2.424.
Lutz, K., Jacobeit, J., Rathmann, J., 2015. Atlantic warm and cold water events and impact on African west coast precipitation. Int. J. Climatol. 35, 128–141. https://doi.org/10.1002/joc.3969.
Marchesiello, P., McWilliams, J.C., Shchepetkin, A., 2001. Open boundary conditions for long-term integration of regional oceanic models. Ocean Model 3, 1–20. https://doi.org/10.1016/S1463-5003(00)00013-5.
McDougall, T.J., Barker, P.M., Marine, C., Research, A., 2011. Getting Started With TEOS-10 and the Gibbs Seawater (GSW) Oceanographic Toolbox: Version 3.0, Version 3.0. ed. Hobart, Tas.: CSIRO Marine and Atmospheric Research.
Mohrholz, V., Schmidt, M., Lutjeharms, J.R.E., 2001. The hydrography and dynamics of the Angola-Benguela Frontal Zone and environment in April 1999: BENEFIT Marine Science. South Afr. J. Sci. 97, 199–208.
Moloney, C.L., Fennessy, S.T., Gibbons, M.J., Roychoudhury, A., Shillington, F.A., Heyden, B.P. von der, Watermeyer, K., 2013. Reviewing evidence of marine ecosystem change off South Africa. Afr. J. Mar. Sci. 35, 427–448. https://doi.org/10.2989/1814232X.2013.836135.
Monteiro, P.M.S., van der Plas, A.K., 2006. 5 Low oxygen water (LOW) variability in the Benguela system: key processes and forcing scales relevant to forecasting, in: Shannon, V., Hempel, G., Malanotte-Rizzoli, P., Moloney, C., Woods, J. (Eds.). Benguela Predicting a Large Marine Ecosystem. Elsevier, Large Marine Ecosystems, pp. 71–90.
Monteiro, P.M.S., van der Plas, A.K., Mélice, J.-L., Florenchie, P., 2008. Interannual hypoxia variability in a coastal upwelling system: ocean–shelf exchange, climate and ecosystem-state implications. Deep Sea Res. Part Oceanogr. Res. Pap. 55, 435–450. https://doi.org/10.1016/j.dsr.2007.12.010.
Monteiro, P.M.S., Dewitte, B., Scranton, M.I., Paulmier, A., Van der Plas, A., 2011. The role of open ocean boundary forcing on seasonal to decadal-scale variability and long-term change of natural shelf hypoxia. Environ. Res. Lett. 1–14. https://doi.org/10.1088/1748-9326/6/2/025002.
Moroshkin, K.V., Bunov, V.A., Bulatov, R.P., 1970. Water circulation in the eastern South Atlantic Ocean. Oceanology 10, 27–34.
Mosquera-Vásquez, K., Dewitte, B., Illig, S., 2014. The Central Pacific El Niño intraseasonal Kelvin wave. J Geophys Res Oceans 119, 6605–6621. https://doi.org/10.1002/2014JC010044.
Ostrowski, M., 2007. Impact of Equatorial Kelvin Waves on Aggregations of Sardinellas (Sardinella spp.) in Angolan Waters. (Working Paper). ICES.
Ostrowski, M., da Silva, J.C.B., Bazik-Sangolay, B., 2009. The response of sound scatterers to El Niño- and La Niña-like oceanographic regimes in the southeastern Atlantic. ICES J. Mar. Sci. 66, 1063–1072. https://doi.org/10.1093/icesjms/fsp102.
Penven, P., Debreu, L., Marchesiello, P., McWilliams, J.C., 2006. Evaluation and application of the ROMS 1-way embedding procedure to the Central California upwelling system. Ocean Model 12, 157–187. https://doi.org/10.1016/j.ocemod.2005.05.002.
Picaut, J., 1983. Propagation of the seasonal upwelling in the eastern equatorial Atlantic. J. Phys. Oceanogr. 13, 18–37. https://doi.org/10.1175/1520-0485(1983)013<0018:POTSUI>2.0.CO;2.
Polo, I., Lazar, A., Rodriguez-Fonseca, B., Arnault, S., 2008. Oceanic Kelvin waves and tropical Atlantic intraseasonal variability: 1. Kelvin wave characterization. J. Geophys. Res. 113, C07009. https://doi.org/10.1029/2007JC004495.
Quiñones, R.A., 2010. Eastern boundary current systems. In: Liu, K.-K., Atkinson, L., Quiñones, R., Talaue-McManus, L. (Eds.), Carbon and Nutrient Fluxes in Continental Margins: A Global Synthesis. Global Change – The IGBP Series. Springer, Berlin Heidelberg, Berlin, Heidelberg, pp. 25–120. https://doi.org/10.1007/978-3-540-92735-8_2.
Richter, I., Behera, S.K., Masumoto, Y., Taguchi, B., Komori, N., Yamagata, T., 2010. On the triggering of Benguela Niños: remote equatorial versus local influences. Geophys. Res. Lett. 37, L20604. https://doi.org/10.1029/2010GL044461.
Rouault, M., 2012. Bi-annual intrusion of tropical water in the northern Benguela upwelling. Geophys. Res. Lett. 39. https://doi.org/10.1029/2012GL052099.
Rouault, M., Florenchie, P., Fauchereau, N., Reason, C.J.C., 2003. South East tropical Atlantic warm events and southern African rainfall. Geophys. Res. Lett. 30, 8009. https://doi.org/10.1029/2002GL014840.
Rouault, M., Illig, S., Bartholomae, C., Reason, C.J.C., Bentamy, A., 2007. Propagation and origin of warm anomalies in the Angola Benguela upwelling system in 2001. J. Mar. Syst. 68, 473–488. https://doi.org/10.1016/j.jmarsys.2006.11.010.
Rouault, M., Servain, J., Reason, C.J.C., Bourlès, B., Rouault, M.J., Fauchereau, N., 2009. Extension of PIRATA in the tropical South-East Atlantic: an initial one-year experiment. Afr. J. Mar. Sci. 31, 63–71. https://doi.org/10.2989/AJMS.2009.31.1.5.776.
Rouault, M., Illig, S., Lübbecke, J., Koungue, R.A.I., 2018. Origin, development and demise of the 2010–2011 Benguela Niño. J. Mar. Syst., Benguela: Opportunity, Challenge and Change 188, 39–48. https://doi.org/10.1016/j.jmarsys.2017.07.007.
Shannon, L.V., Nelson, G., 1996. The Benguela: large scale features and processes and system variability. In: The South Atlantic. Springer Berlin Heidelberg, pp. 163–210.
Shannon, L.V., Boyd, A.J., Brundrit, G.B., Taunton-Clark, J., 1986. On the existence of an El Niño-type phenomenon in the Benguela System. J. Mar. Res. 44, 495–520. https://doi.org/10.1357/002224086788403105.

Shchepetkin, A.F., McWilliams, J.C., 2005. The regional oceanic modeling system (ROMS): a split-explicit, free-surface, topography-following-coordinate oceanic model. Ocean Model 9, 347–404. https://doi.org/10.1016/j.ocemod.2004.08.002.

Shillington, F.A., 1998. The Benguela upwelling system off southwestern Africa. In: The Global Coastal Ocean (Ed.), Regional Studies and Syntheses. The Sea. Wiley, New-York, pp. 583–604.

Shillington, F.A., Reason, C.J.C., Duncombe Rae, C.M., Florenchie, P., Penven, P., 2006. 4 Large scale physical variability of the Benguela Current Large Marine Ecosystem (BCLME), in: Shannon, V., Hempel, G., Malanotte-Rizzoli, P., Moloney, C., Woods, J. (Eds.). Benguela Predicting a Large Marine Ecosystem. Elsevier, Large Marine Ecosystems, pp. 49–70.

Siegfried, L., Schmidt, M., Mohrholz, V., Pogrzeba, H., Nardini, P., Böttinger, M., Scheuermann, G., 2019. The tropical-subtropical coupling in the Southeast Atlantic from the perspective of the northern Benguela upwelling system. PLoS One 14, e0210083. https://doi.org/10.1371/journal.pone.0210083.

Sowman, M., Cardoso, P., 2010. Small-scale fisheries and food security strategies in countries in the Benguela Current Large Marine Ecosystem (BCLME) region: Angola. Namibia and South Africa. Mar. Policy 34, 1163–1170. https://doi.org/10.1016/j.marpol.2010.03.016.

Strub, P.T., Shillington, F.A., James, C., Weeks, S.J., 1998. Satellite comparison of the seasonal circulation in the Benguela and California current systems. Afr. J. Mar. Sci. 19.

Tchipalanga, P., Dengler, M., Brandt, P., Kopte, R., Macuéria, M., Coelho, P., Ostrowski, M., Keenlyside, N.S., 2018. Eastern boundary circulation and hydrography off Angola: building Angolan oceanographic capacities. Bull. Am. Meteorol. Soc. 99, 1589–1605. https://doi.org/10.1175/BAMS-D-17-0197.1.

Woodhead, Hamukuaya, H., O'Toole, M.J., Stroemme, T., Kristmannsson, S., 1997a. Recruit mortalities in Cape hake, following exclusion from shelf habitat by persistent hypoxia in the Benguela Current, Namibia. In: Physical-Biological Interactions. Presented at the ICES International Symposium, Recruitment Dynamics of Exploited Marine Populations, pp. 26–27.

Woodhead, Hamukuaya, H., O'Toole, M.J., Stroemme, T., Saetersdal, G., Reiss, M., 1997b. Catastrophic loss of two billion Cape hake recruits during widespread anoxia in the Benguela Current off Namibia. In: Physical-Biological Interaction. Presented at the ICES International Symposium, Recruitment Dynamics of Exploited Marine Populations, pp. 105–106.

Woodhead, P.M., Hamukuaya, H., O'Toole, M.J., McEnroe, M., 1998. Effects of oxygen depletion in shelf waters on hake populations off central and northern Namibia, International Symposium, Environmental Variability in the South East Atlantic. NATMIRC, Namibia.

Supporting Information for

"Interannual Coastal Trapped Waves in the Angola-Benguela Upwelling System and Benguela Niño and Niña events"

M.-L. Bachèlery[a,b], S. Illig[c,a], and M. Rouault[a,b]

[a] Department of Oceanography, MARE Institute, LMI ICEMASA, University of Cape Town, Rondebosch, South Africa

[b] Nansen-Tutu Centre for Marine Environmental Research, University of Cape Town, Rondebosch, South Africa

[c] Laboratoire d'Etudes en Géophysique et Océanographie Spatiale (LEGOS), CNRS/IRD/UPS/CNES, Toulouse, France

Contents

Introduction

This supporting information provides the description of the *in situ*, remote-sensed observations and reanalysis outputs used in this study, along with a validation of our regional model configuration.

S1 Datasets information

A set of available data is used to force and compare our model outputs to the observed conditions.

S1.1 *In situ* data

Nansen cruises: *In situ* temperature and salinity profiles from the R/V Dr. Fridtjof Nansen cruises (Tchipalanga et al., 2018) were used to evaluate the mean state of the control

run simulation (ROMS-CR) along the south-western African coast. Measurements were collected biannually along the Angolan coast from 5°S to 18°S, between 1995 and 2015. Mean state conditions were obtained by averaging all the available profiles. Datasets are available throughout the world data center PANGAEA at https://doi.pangaea.de/10.1594/PANGAEA.886492/.

PIRATA mooring: We use monthly **i**nterannual **S**ea **S**urface **T**emperature (**iSST**) anomalies from *in situ* PIRATA mooring records (Bourles et al., 2008; Servain et al., 1998) deployed at [0°E; 0°N] over the 1998–2008 period to evaluate the interannual variability of ROMS-CR. Data, gridding procedure and climatology estimations are available at http://www.pmel.noaa.gov/tao/disdel/.

S1.2 Satellite data

Sea Level Anomalies (SLA): We use the weekly gridded AVISO combined product for SLA, provided by the Ocean Topography EXperiment TOPEX/Poseidon/Jason and the European Remote Sensing Satellite ERS-1/2 data sets, from January 1993 up to December 2008 on a 1/3° Mercator grid (Ducet et al., 2000; Le Traon et al., 1998). Data can be downloaded from Aviso+ data server at http://www.aviso.altimetry.fr/en/data/products/.

Sea Surface Temperature (SST): Daily SST observations from 1993 to 2008 with a spatial resolution of 0.25°x0.25° was acquired from a Group for High-Resolution Sea Surface Temperature (GHRSST; Reynolds et al., 2007). The product merges SST observations from different sources that are interpolated and extrapolated using Optimal Interpolation (OI) at the NOAA National Centers for Environmental Information. The main source of SST data comes from remote-sensed AVHRR observations and *in situ* platforms such as ships and buoys. Datasets are available at https://podaac.jpl.nasa.gov/dataset/AVHRR_OI-NCEI-L4-GLOB-v2.0/.

Current: The gridded satellite-based ocean current data GlobCurrent product (Version 2.0) is used in this study to analyse the simulated interannual surface zonal and meridional currents variabilities (Rio et al., 2014). 3 hourly surface currents outputs are provided with a 0.25°x0.25° horizontal grid resolution over 1993-2008 period. Data are available at http://www.ifremer.fr/opendap/cerdap1/globcurrent/.

S1.3 Reanalysis products

Oceanic Reanalysis: 5-day averages of the Simple Ocean Data Assimilation (SODA) v2.1.6 outputs mapped onto a regular 0.5°×0.5°×40-level grid (19 vertical levels in the upper 500 m depth) are prescribed as initial and open lateral boundary conditions for our regional ocean model simulations. SODA combines the Los Alamos implementation of the POP (Parallel Ocean Program) model with a sequential estimation data assimilation method (Carton et al., 2000; Carton and Giese, 2008). The version used for this paper (SODA 2.1.6) is forced by outputs from the European ReAnalysis-40 (ERA-40) from 1958 to 2001 and then by ERA-Interim for the period spanning from 2002 to 2008. SODA 2.1.6 assimilates all available data from hydrographic stations, expendable bathythermographs, and floats, but does not use satellite altimetry. In this version, hydrographic observations come from WOD09 (Boyer et al., 2009) using their standard level temperature and salinity data. Data can be downloaded at http://soda.tamu.edu/data.htm/.

Atmospheric Reanalysis: The global forcing datasets Drakkar Forcing Set version 5.2 (DFS5.2; Dussin et al., 2014) is used for the atmospheric forcing of our ocean simulations. The DFS5.2 data set has been built by combining the ERA40 (1958-1978) and ERA-interim (1979-2015) atmospheric reanalysis (Dee et al., 2011) with applied corrections on temperature and wind fields as well as heat and water fluxes using observed datasets, satellite-based products, and global ORCA ocean model configurations. 3 hourly wind and daily long- and shortwave radiation and precipitation fields were acquired from 1958 to 2008 at a horizontal resolution of 0.7°x0.7°.

S2 Evaluation of the model performances

Here, we assess the realism of the control-run simulation (ROMS-CR) in reproducing the oceanic conditions of the south-eastern Atlantic. We evaluate the mean state and the interannual variability along the equatorial waveguide and in the coastal fringe off south-western Africa. We focus our analysis on the key parameters related to the ocean dynamics and relevant for our study, *i.e.* SLA, surface zonal and meridional currents, SST and the sub-surface temperature.

The realism of the modelled mean SST is evaluated against the GHRSST remote-sensed data over the 1993-2008 period (Fig. S1), which corresponds to the period covered by the

observations (see Section S1.2). The model realistically represents the mean distribution of the heat in the south-eastern Atlantic Ocean characterised by warm waters over the tropics that progressively cool toward the pole. Worthy of note also, is the **B**enguela **U**pwelling **S**ystem (**BUS**) along the south-west coast of Africa between [18°S-34°S] which exhibits cold surface waters on a 200 km coastal band (Fig. S1a). Maximum differences between modelled and observed SST remains below 2°C (Fig. S1b). Two small patches of too warm SST are depicted along the south-west coast of Africa. The first patch is stretched between [16°S-17°S] in the **A**ngola-**B**enguela **F**rontal **Z**one (**ABFZ**), where sharp meridional temperature gradients are observed. The bias is most likely associated with a latitudinal shift in the mean position of the ABFZ (Fig. S1a). The second maximum is located in the **N**orthern part of **BUS** (**NBUS**) between [22°S-26°S]. This bias is likely to be associated with a too weak nearshore wind stress curl that characterised the DFS5.2 wind product used to force ROMS-CR (*Veitch., pers comm*). Over the rest of the domain, SST bias remains smaller than 1°C. The model mean state is further evaluated by comparing vertical profiles of the temperature over the 1995-2008 period to the Nansen *in situ* observations at 3 different locations [5°S-8°S] (Fig. S1c), [10°S-13°S] (Fig. S1d), [14°S-18°S] (Fig. S1e) along the south-west coast of the African continent. For consistency, the model temperature profile has been depicted at the exact same location and time than the *in situ* observations. Overall, the mean vertical temperature structure is really well represented by the model. Again, the most significant bias (~2.5°C) is found in the ABFZ region in the first 50m. Note as well that, in this region, the mean position of the thermocline in ROMS-CR is deeper (~20m) than in the observations.

We now evaluate the interannual SST, SLA and surface currents variabilities in ROMS-CR. Please refer to Section 2.1 of the manuscript for a complete description of the methodology used to calculate interannual anomalies. Fig. S2a illustrates the good coherence between the iSST anomalies of ROMS-CR, GHRSST and PIRATA *in-situ* data along the equator at 0°E. All the time series exhibits noticeable interannual fluctuations with comparable level of energy. The model is skillful in capturing the observed iSST variability as well as most of the extreme events. The correlation coefficient between modelled SST and the remote-sensed observations is 0.67. We further assess the realism of the simulated equatorial and coastal interannual fluctuations by comparing them to satellite observations over the 1993-2008 period and summarising them using a Taylor diagram (Taylor, 2001). Fig. S2b presents ROMS-CR skills in realistically simulating iSST (square) and **i**nterannual **SLA** (**iSLA**; circle) along the equator (averaged within [1°S-1°N]) and along the south-west African coast (averaged within the 1°-width coastal band) as compared to the GHRSST and the AVISO remote-sensed interannual

variability, respectively. Colours indicate the longitude along the equator and the latitude along the coast. Note that along the west African coast, time series are preliminarily smoothed using a 5°-width latitudinal running filter, to remove any remaining mesoscale variability. Results show a very good agreement between the ROMS-CR and the observations for both, the iSLA and iSST variabilities with a fair estimation of the energy of the interannual activity. Taylor scores (*cf.* Eq. (4) of Taylor, 2001) along the equatorial waveguide and the south-western coast of Africa for iSLA and iSST are very good, ranging between 0.65-0.85 and 0.8-0.92, respectively. However, modelled iSLA fluctuations at the equator between 10°W and 0°E are slightly more energetic than the altimetric estimations. Also, of interest is the fact that there is a gradual reduction of the consistency between ROMS-CR outputs and AVISO data with latitude poleward (circle in Fig. S2b). In the BUS, the lack of agreement between ROMS-CR and the altimetric observations can be attributed to meso-scale activity. In the absence of data assimilation in our configuration, simulated and observed eddies cannot be collocated in time and space. Finally, similarly to Fig. S2b, Fig. S2c provides a Taylor diagram that includes the evaluation of the modelled interannual equatorial zonal (averaged within [1°S-1°N]) and coastal (averaged within the 1°-width coastal band) meridional currents anomalies for each longitude along the equator and latitude along the south-west African coast, respectively. Modelled currents are compared to the GlobCurrent satellite product over the 1993-2008 period. Results show the good statistical consistency between model and observations with correlations above the 95% confident level threshold. ROMS-CR interannual meridional current anomalies agree best with the altimetric data between [12°S-34°S], with Taylor scores ~0.75, correlation coefficients >0.5 and the normalized standard deviation comprised between 0.8 and 1.2.

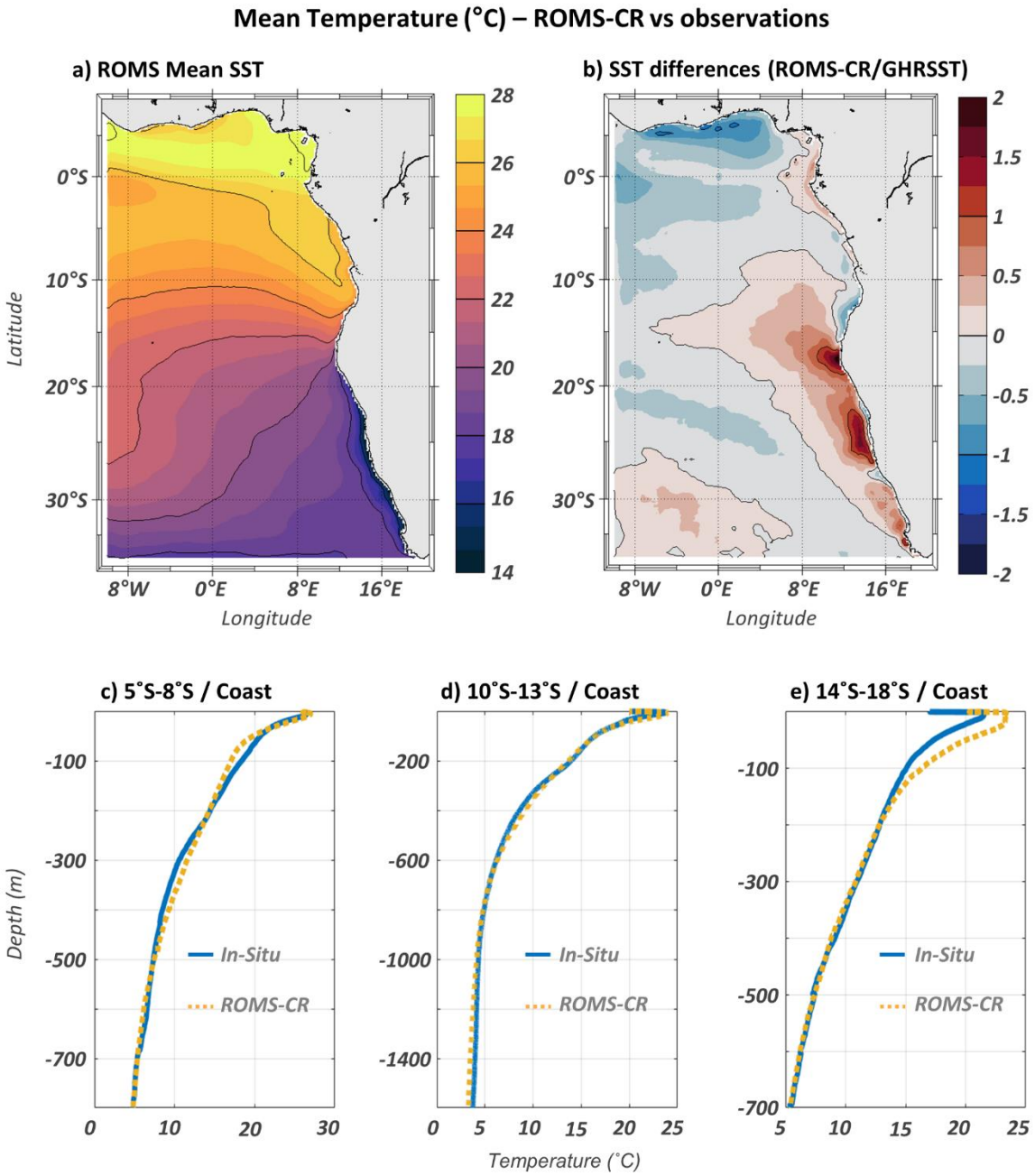

Fig. S1: ROMS-CR performances in simulating the mean ocean conditions. a) Map of mean (1993-2008) ROMS-CR **S**ea **S**urface **T**emperature (**SST**), and b) differences between model and GHRSST SST. c-e) Mean (1995-2008) vertical temperature profile averaged within a 0.5° coastal width band at c) [5°S-8°S] d) [10°S-13°S] e) [14°S-18°S] for the Nansen *in situ* data (blue plain line) and ROMS-CR model outputs (yellow dash line). Unit is °C.

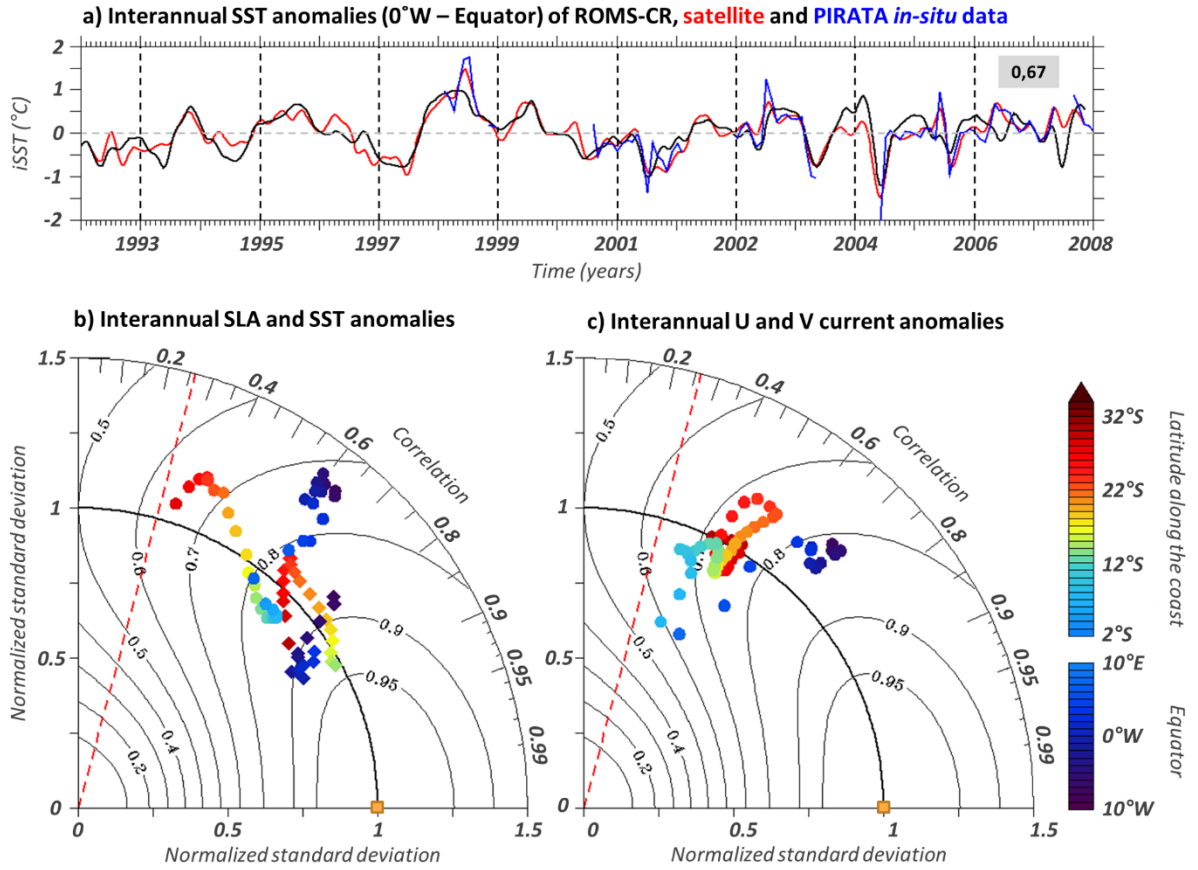

Fig. S2: ROMS-CR performances in simulating the interannual variability. a) Time-series of detrended **i**nterannual **S**ea **S**urface **T**emperature (**iSST**; °C) anomalies averaged at [0°W; 0°N] of ROMS-CR (black), remote sensed GHRSST (red) and PIRATA *in situ* (blue) data. b**)** Normalized Taylor diagram (Taylor, 2001) summarizing the model skills in simulating the detrended **i**nterannual **S**ea **L**evel **A**nomalies (**iSLA**; circle) and iSST (square) variabilities versus remote-sensed AVISO and GHRSST data along the equator (averaged within [1°S-1°N]) and along the south-western coast of Africa (averaged within the 1°-width coastal fringe) over 1993-2008. Colours indicate the longitude along the equator and the latitude along the south-west African coast. To remove the meso-scale variability, time series are preliminary smoothed using a 5°-width latitudinal running filter. Isolines provide a measure of the skill as defined by Eq. (4) from Taylor, (2001). c) Same as panel (b) illustrating the model skills in representing the detrended interannual zonal (meridional) current variability along the equator averaged within [1°S-1°N] (along the south-western coast of Africa averaged within the 1°-width coastal fringe) compared to the GlobCurrent data.

References

Bourles, B., Lumpkin, R., McPhaden, M.., Hernandez, F., Nobre, P., Campos, E., Servain, J., 2008. THE PIRATA PROGRAM. Bull. Am. Meteorol. Soc. 89, 1111–1125.

Boyer, T.., Antonov, J.I., Baranova, O.K., Garcia, H.E., Johnson, D.R., Locarnini, R.A., Mishonov, A.V., Seidov, D., Smolyar, I.V., Zweng, M.M., 2009. World Ocean Database 2009, Chapter 1: Introduction, in: NOAA Atlas NESDIS., 66. U.S. Gov. Printing Office, Wash., D.C.

Carton, J.A., Chepurin, G., Cao, X., Giese, B., 2000. A Simple Ocean Data Assimilation Analysis of the Global Upper Ocean 1950–95. Part I: Methodology. J Phys Ocean. 30, 294–309. https://doi.org/10.1175/1520-0485(2000)030<0294:ASODAA>2.0.CO;2

Carton, J.A., Giese, B.S., 2008. A Reanalysis of Ocean Climate Using Simple Ocean Data Assimilation (SODA). Mon Wea Rev 136, 2999–3017. https://doi.org/10.1175/2007MWR1978.1

Dee, D.P., Uppala, S.M., Simmons, A.J., Berrisford, P., Poli, P., Kobayashi, S., Andrae, U., Balmaseda, M.A., Balsamo, G., Bauer, P., Bechtold, P., Beljaars, A.C.M., van de Berg, L., Bidlot, J., Bormann, N., Delsol, C., Dragani, R., Fuentes, M., Geer, A.J., Haimberger, L., Healy, S.B., Hersbach, H., Hólm, E.V., Isaksen, L., Kållberg, P., Köhler, M., Matricardi, M., McNally, A.P., Monge-Sanz, B.M., Morcrette, J.-J., Park, B.-K., Peubey, C., de Rosnay, P., Tavolato, C., Thépaut, J.-N., Vitart, F., 2011. The ERA-Interim reanalysis: configuration and performance of the data assimilation system. QJR Meteorol Soc 137, 553–597. https://doi.org/10.1002/qj.828

Ducet, N., Le Traon, P.Y., Reverdin, G., 2000. Global high-resolution mapping of ocean circulation from TOPEX/Poseidon and ERS-1 and -2. J Geophys Res 105, 19477–19498. https://doi.org/10.1029/2000JC900063

Dussin, R., Barnie, B., Brodeau, L., 2014. The making of Drakkar forcing set DFS5.

Le Traon, P.Y., Nadal, F., Ducet, N., 1998. An Improved Mapping Method of Multisatellite Altimeter Data. J Atmos Ocean. Technol 15, 522–534. https://doi.org/10.1175/1520-0426(1998)015<0522:AIMMOM>2.0.CO;2

Reynolds, R.W., Smith, T.M., Liu, C., Chelton, D.B., Casey, K.S., Schlax, M.G., 2007. Daily High-Resolution-Blended Analyses for Sea Surface Temperature. J Clim. 20, 5473–5496. https://doi.org/10.1175/2007JCLI1824.1

Rio, M.-H., Mulet, S., Picot, N., 2014. Beyond GOCE for the ocean circulation estimate: Synergetic use of altimetry, gravimetry, and in situ data provides new insight into

geostrophic and Ekman currents. Geophys. Res. Lett. 41, 8918–8925. https://doi.org/10.1002/2014GL061773

Servain, J., Busalacchi, A., McPhaden, M.., Moura, A.., Reverdin, G., Vianna, M., Zebiak, S.., 1998. A pilot research moored array in the tropical Atlantic (PIRATA). Bull. Am. Meteorol. Soc. 79, 2019–2031.

Taylor, K.E., 2001. Summarizing multiple aspects of model performance in a single diagram. J Geophys Res 106, 7183–7192. https://doi.org/10.1029/2000JD900719

Tchipalanga, P., Dengler, M., Brandt, P., Kopte, R., Macuéria, M., Coelho, P., Ostrowski, M., Keenlyside, N.S., 2018. Eastern Boundary Circulation and Hydrography Off Angola: Building Angolan Oceanographic Capacities. Bull. Am. Meteorol. Soc. 99, 1589–1605. https://doi.org/10.1175/BAMS-D-17-0197.1